LITHOS 512-513 (2025) 108156

Contents lists available at ScienceDirect

LITHOS

journal homepage: www.elsevier.com/locate/lithos

A sheared garnet peridotite mantle xenolith from the Delitzsch Carbonatite Complex, Germany - Evidence for thickened Cretaceous lithosphere beneath Central Europe

Tobias Röper [a,*], Yannick Bussweiler [a], Max Hellers [a], Frank Möckel [b], Frank Wombacher [a], Carsten Münker [a]

[a] Institute of Geology and Mineralogy, University of Cologne, Germany
[b] Wismut GmbH, Chemnitz, Germany

ARTICLE INFO

Keywords:
Delitzsch Carbonatite complex
Ultramafic lamprophyre
Mantle xenolith
Sheared peridotite
Subcontinental lithospheric mantle
Delamination

ABSTRACT

Sheared garnet peridotites occur in the deep lithosphere and record processes of deformation, melt interaction, and metasomatism along the lithosphere-asthenosphere boundary (LAB). While sheared peridotites are typically found in kimberlites and related volcanic rocks within cratonic settings, this study reports on an exceptionally fresh occurrence found in an ultramafic lamprophyre (UML) from the Delitzsch Carbonatite Complex (DCC) in Saxony, Germany. The xenolith was emplaced during the main magmatic activity, previously dated to between 72 and 83 Ma during the late Cretaceous period. The xenolith contains porphyroclasts of garnet, clinopyroxene and orthopyroxene in a fine-grained matrix of olivine, and thus classifies as garnet-lherzolite. Evidence of deformation and metasomatism is recorded in its mosaic to fluidal mosaic texture, characterized by olivine neoblasts, elongated garnet grains, and reaction rims around garnet (kelyphite) and clinopyroxene (spongy rims). The xenolith represents a relatively fertile mantle composition with magnesium numbers (Mg# = Mg/[Mg + Fe^{2+}] × 100) of 89.4 for olivines and clinopyroxenes, 90.8 for orthopyroxenes and 82.6 for garnets. Measured trace element compositions suggest high temperature interaction with primitive, fertile melts, as shown by an enrichment of middle rare earth elements (MREE) as well as high field strength elements (HFSE) such as Ti. Reconstructed P-T conditions indicate equilibration at 61.1 ± 5.1 kbar and 1330 ± 23 °C. The corresponding depth of ~190 km is substantially deeper than the depth of the modern LAB at 120-140 km. This not only establishes the sheared garnet peridotite xenolith as the deepest sample ever recorded from Germany but also has significant implications for mantle dynamics beneath the Mesozoic Central European crust. The sheared garnet peridotite provides evidence of the destabilization and destruction (e.g., by delamination) of a formerly thick lithosphere at least beneath Eastern Germany and possibly beneath Central Europe. Such thick, craton-like lithosphere could have originally underlain the Bohemian Massif and extended to the NW at upper mantle depth.

1. Introduction

Sheared peridotites are samples from the lithosphere-asthenosphere boundary (LAB), originating from the transitional zone between non-convecting to convecting mantle. Early studies focused on sheared peridotites found in cratonic kimberlites in South Africa and Lesotho and investigated them to identify the location of the low-velocity zone between the lithosphere and asthenosphere (Boyd and Nixon, 1975). Furthermore, their textures were compared to those from recrystallisation experiments to determine average melt intrusion velocities of kimberlites (Mercier, 1979). Modern studies explore the role of sheared peridotites in metasomatism and their connection to the destabilization of the lower lithosphere by carbonate-rich (e.g., proto-kimberlitic) melts (Braga et al., 2024; Heckel et al., 2023; O'Reilly and Griffin, 2010). Although most sheared peridotites are found in kimberlites or other deep-seated, carbonate-bearing rocks, they have also been found in basaltic rocks (Ashchepkov et al., 2011). Current models suggest that sheared peridotite xenoliths record the process of lithosphere destruction, as witnessed in the São Francisco craton in Brazil (Braga et al., 2024), in the Kaapvaal craton (e.g., Heckel et al., 2023, 2022) as well as

* Corresponding author.
E-mail address: tobiasroeperde@gmail.com (T. Röper).

https://doi.org/10.1016/j.lithos.2025.108156
Received 6 January 2025; Received in revised form 29 May 2025; Accepted 5 June 2025
Available online 18 June 2025

in the North China craton (e.g., Chen et al., 2023; Liu et al., 2018; Zhu et al., 2011).

This study investigates a sheared garnet peridotite mantle xenolith found within an ultramafic lamprophyre (UML) from the Delitzsch Carbonatite Complex (DCC). The sample was recovered during drilling projects conducted in the 1970s and '80s (see Möckel, 2023 for details). The DCC itself is covered by over 100 m of sediments and only sampled through drill cores. Thus, very limited material is available of the UMLs and even less so of their mantle cargo, making this sheared peridotite sample exceptionally rare and special. The key issues addressed in this article include: (1) how texture and composition compare to other sheared peridotite occurrences, (2) which mantle processes are responsible for its formation and exhumation, and (3) how these processes fit within the regional geodynamic setting and tectonic history.

To this end, we present detailed petrographic observations, and mineral chemistry data for olivine, orthopyroxene, clinopyroxene, and garnet determined by electron probe microanalysis (EPMA) for major elements, and by laser ablation-inductively coupled plasma-mass spectrometry (LA-ICP-MS) for trace elements. By combining all the gathered information, modal and bulk compositions are estimated. Several geothermobarometers are applied to estimate the P-T conditions of equilibration.

2. Geological setting

Delitzsch and the adjacent DCC are located 20 km north of Leipzig, located on Saxothuringian basement near the southern edge of the Mid-German Crystalline Zone (MGCZ) (Fig. 1).

The Variscan orogeny marks a significant orogenic event during which Laurussia to the north collided with Gondwana to the south. The orogeny commenced by the Early Devonian (around 400 Ma) and lasted until the Late Carboniferous (around 300 Ma) (e.g., Kroner and Romer, 2013). At the onset of the orogeny, the Saxothuringian microterrane was subducted beneath the Moldanubian Massif, which constituted part of Gondwana. This was followed by the closure of the Rheic Ocean and the subduction of rhenohercynian oceanic lithosphere. The Rhenohercynian Zone mainly comprises marine sediments from the Rheic Ocean. This is opposed to the ancient core of the Saxothuringian Zone which consists of Cadomian continental crust from the Proterozoic to early Phanerozoic (Jones et al., 2010). The MGCZ, which formed as part of the volcanic arc and accretionary wedge between these terranes, represents the suture between the subducted Rhenohercynian oceanic lithosphere and the overriding Saxothuringian Zone (Franke, 2000). These orogenic events have led to substantial thickening of the lithosphere. (e.g., Hillenbrand and Williams, 2022; Konopásek and Schulmann, 2005).

Following the collision of the Eurasian and African plates during the Alpine orogeny in the Late Cretaceous, complex stress fields developed in Central Europe, leading to widespread uplift and the reactivation of Variscan fault systems (Krüger et al., 2013). The magmatism of the DCC can be linked to activities along two main structural zones: the *E*-W trending Delitzsch-Doberlug Syncline and the N-S trending Plauen-Leipzig-Dessau Zone (Seifert, 2000). A total of six distinct phases of volcanic activity have been identified in the DCC, given here in chronological order (Krüger et al., 2013): 1. intrusion of a carbonatitic magma body; 2. intrusion of ultramafic and alkali lamprophyres; 3. formation of diatremes ('intrusive breccia'); 4. intrusion of lamprophyres within diatremes of stage 3; 5. formation of beforsite dikes; 6. formation of carbonatite dikes. The main period of magmatic activity ranged from 83 Ma until 72 Ma (Möckel, 2023).

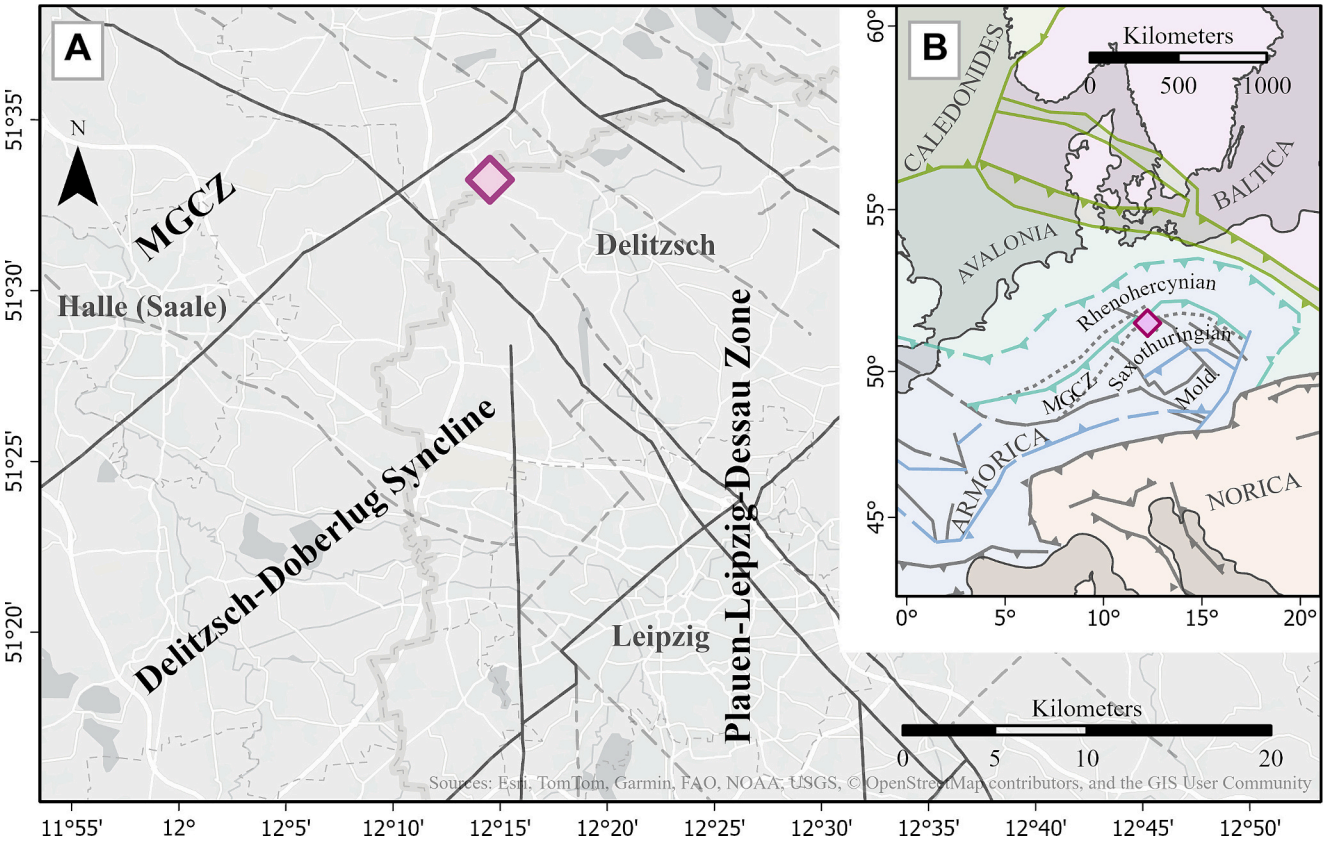

Fig. 1. A: Area around Delitzsch with relevant fault systems and location of the Mid-German Crystalline Zone (MGCZ). Fault data provided by the Saxon State Office for Environment, Agriculture and Geology. B: Overview of the Central European Variscides (after Franke, 2006). The purple diamond marks the drilling site of the core from which the sample was obtained. (For interpretation of the references to colour in this figure legend, the reader is referred to the web version of this article.)

3. Samples and methods

3.1. Origin of samples

The original sample investigated had dimensions of approximately 2 × 3 × 0.5 cm (Fig. 2). From 1971 to 1989, SDAG Wismut prospected the area around Delitzsch for uranium deposits (cf. Möckel, 2023). During prospecting, drill cores were taken and assigned a running number along with the year the core was extracted. This study analyzes a garnet peridotite mantle xenolith from the drill site Wis BAW 736/77, located just east of the Serbitz district of Wiedemar at coordinates N 51° 33' 21.085", E 12° 14' 21.787" (Fig. 1). The xenolith was extracted from a depth of 456.2 m. The host rock is a UML-diatreme breccia of alnöite composition (i.e. melilite-bearing), suggesting emplacement occurred during phase 3 of the DCC activity (Krüger et al., 2013; Möckel, 2023).

Two thick sections (80-100 μm) were prepared, consuming the entire sample in the process. Due to the limited amount of sample material and its pre-specified shape, the sections had to be oriented parallel to the original sample surface. Both sections were polished before further analysis. Thick sections were chosen over thin sections for this study to ensure sufficient material was available for spot analysis by LA-ICP-MS (see below).

3.2. Analytical methods

The prepared thick sections were graphite-coated by vacuum deposition using a Quorum Q150T ES coating machine. A JEOL JXA 8900RL electron microprobe at the Institute of Geology and Mineralogy, University of Cologne was used to determine the chemical composition of the minerals. Backscattered electron (BSE) imaging was used for identification of zoning or changes in chemical composition within the same phase. Energy dispersive spectroscopy (EDS) was conducted for mineral identification, aiding in the subsequent quantitative analysis by wavelength dispersive spectroscopy (WDS). For WDS, a TAP crystal was used for Mg, Na, Si, and Al; a LIF crystal for Fe and Mn; a LIFH crystal for Cr, Ni, and Ti; and a PETJ crystal for K and Ca. The calibration for the WDS analyses of olivines and garnets was done using the following Astimex mineral standards olivine (Mg, Fe), jadeite (Na), orthoclase (K), chromite (Cr), almandine (Si, Al), rhodonite (Mn), diopside (Ca) and rutile (Ti), and the P&H standard nickel oxide (Ni). Pyroxenes were calibrated using the same standards, except that olivine was used for Fe, almandine for Al, and diopside for Mg, Si, and Ca. At the beginning and end of the measurement, Cr-diopside and pyrope Astimex standards, and 355OL olivine (Bussweiler et al., 2019) were measured as secondary standards, to detect instrument drift and to monitor accuracy and precision. An accelerating voltage of 20 kV, beam current of 20 nA, and beam size of 2 μm were used for quantitative analysis. Peak and background measuring times were set to 30 s and 15 s for all elements, except K and Na, which were set to 10 s and 5 s, respectively. Background measurements were taken twice for each element (i.e., before and after the peak measurement), so that the total background measurement time matched the peak time.

Trace element measurements were conducted using a ThermoFisher iCAP Q quadrupole ICP-MS operated at 1150 W plasma power in combination with an ESL imageGEO193 laser ablation system at the Institute of Geology and Mineralogy, University of Cologne. The laser was focused on the sample surface with an energy density of 4 J/cm^2 and a spot size of 70 μm. A repetition rate of 6 Hz was used for olivine and 10 Hz for orthopyroxene, clinopyroxene and garnet. The background time was set to 30 s, the ablation time to 40 s. The aerosol was carried from the two-volume ablation chamber by 0.8 L/min He flow to which 0.75 L/min Ar was added via a nebulizer right after the ablation chamber

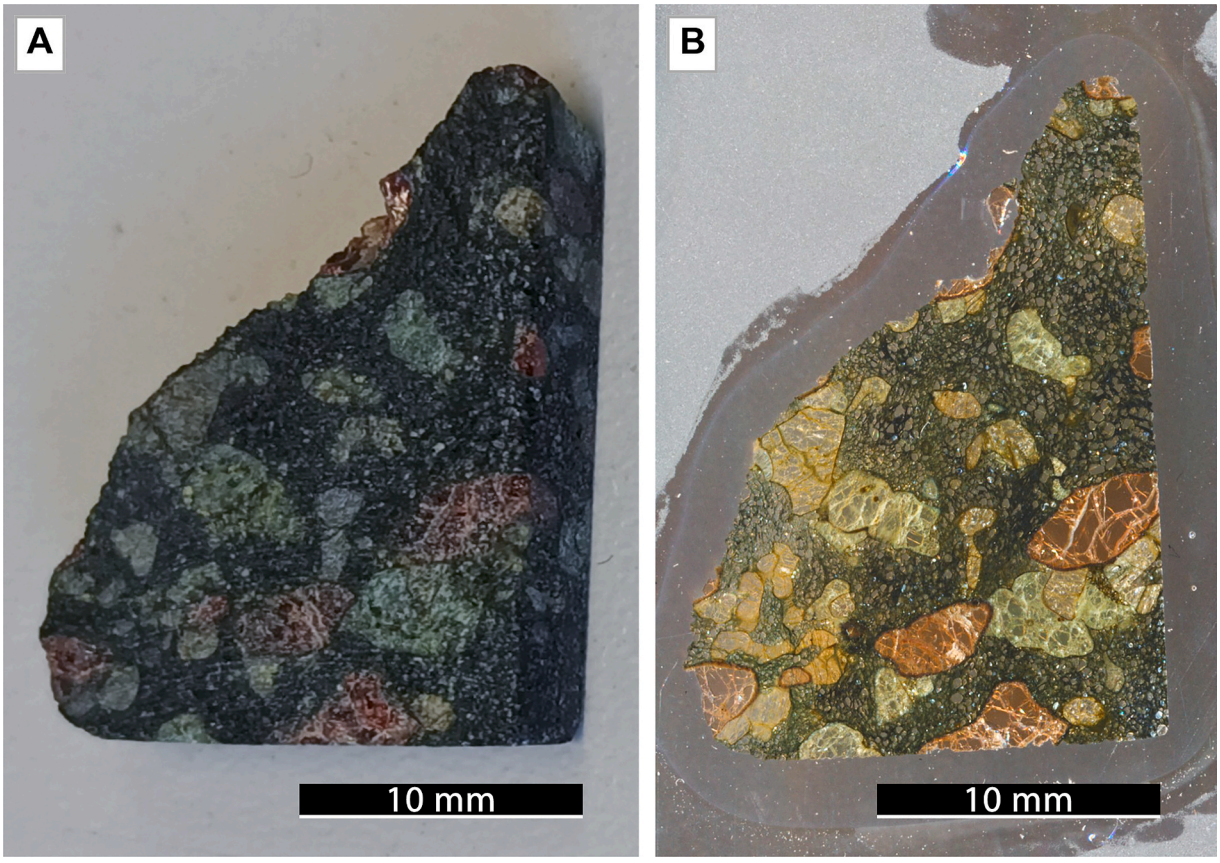

Fig. 2. A: Overview of the analyzed sample as provided. The sample was retrieved from an UML-diatreme breccia from drill core Wis BAW 736/77 (see text for further details). B: Scan of thick section with porphyroclasts of garnet and pyroxene visible to the naked eye in a dark olivine matrix.

within a cyclonic PEEK spray chamber filled with steel wool (Hu et al., 2012) to smooth the signal. A dwell time of 10 ms was selected for the measurement of each isotope. The measured isotopes for olivine, as well as pyroxene and garnet, are listed in the supplementary data (Table S1). NIST SRM 612 was used as the calibration material with ^{29}Si as the internal standard. The reference glass KL2-G (Jochum et al., 2006) and 355OL olivine (Bussweiler et al., 2019) were used to assess the accuracy of the results and to detect any potential drift. These standards were measured periodically throughout the analytical session. Data reduction to obtain the element concentrations was performed using Iolite 4 (Paton et al., 2011).

4. Results

4.1. Petrography

In thin section, the deformed texture of the sample becomes evident (Fig. 2B). The sample can best be described as a sheared garnet peridotite with a porphyroclastic texture. The matrix-forming olivine grains are uniform in size and appearance, ranging from 20 µm to 200 µm (Fig. 3). They are transparent to light green in plane-polarized light (PPL). Grain boundaries appear darker. Olivine grains exhibit a mosaic to slightly fluidal mosaic texture (e.g., Heckel et al., 2022), constituting the bulk of the peridotite. The grains are rounded and anhedral in habitus. Triple junctions with angles around 120° can be observed but are not present at all olivine-olivine boundaries. Comparison to similar garnet peridotites indicates a neoblastic nature (Heckel et al., 2022; Kargin et al., 2017). The olivine crystals exhibit stress features in the form of kink bands under cross-polarized light (CPL). The direction of banding varies between grains, suggesting a growth-related rather than microtectonic origin.

Clinopyroxene and orthopyroxene are scattered throughout the matrix, with grain sizes varying from 200 µm to 1400 µm. Orthopyroxene crystals are beige or light brown in colour, whereas clinopyroxene crystals display a sap-green colour (in PPL). Most pyroxene grains are small to medium-sized, whereas a few larger grains show more fracturing and signs of alteration. No clear orientation of pyroxenes is apparent. Cleavage planes are well-developed, particularly in orthopyroxene (Fig. 3A). Clinopyroxenes exhibit mostly anhedral shapes, while orthopyroxenes range from anhedral to subhedral. Veins of sulfate and carbonate, apparently following the cleavage planes, are predominantly found within orthopyroxene crystals (e.g., Fig. 3A). Some clinopyroxene grains show signs of resorption or reaction in their rims (Fig. 3B). These rims are similar to spongy rims observed in other sheared peridotites (Braga et al., 2024; Heckel et al., 2023). One clinopyroxene crystal was found to contain another clinopyroxene as inclusion (Fig. 3C). Rutile was found as inclusions in orthopyroxene and as an accessory phase within the olivine groundmass.

The garnet grains show a deep red colour with dark rims in PPL. Their size ranges from 500 µm to 1700 µm. Unlike the other minerals, garnet shows a preferred orientation in the rock; all garnet grains appear elongated and oval-shaped and are oriented in the same general direction. Fine-grained symplectite rims surround all garnets (Fig. 3D) and are composed of different phases. These rims are similar to kelyphite rims observed in other sheared peridotites (e.g., Heckel et al., 2022; Kargin et al., 2021), but due to their fine-grained intergrowth, no quantitative measurements could be obtained.

Images obtained through BSE imaging allow for a more detailed investigation of the observed mineralogical and textural properties of the sample (Fig. 4A). Olivine crystals in both samples show no sign of internal zoning, although grain boundaries of all grains show signs of alteration. EDS analysis identifies the newly formed phases as serpentine and other phyllosilicates (Fig. 4B). Serpentinization is limited to the grain boundaries and a high proportion of fresh olivine remains. All

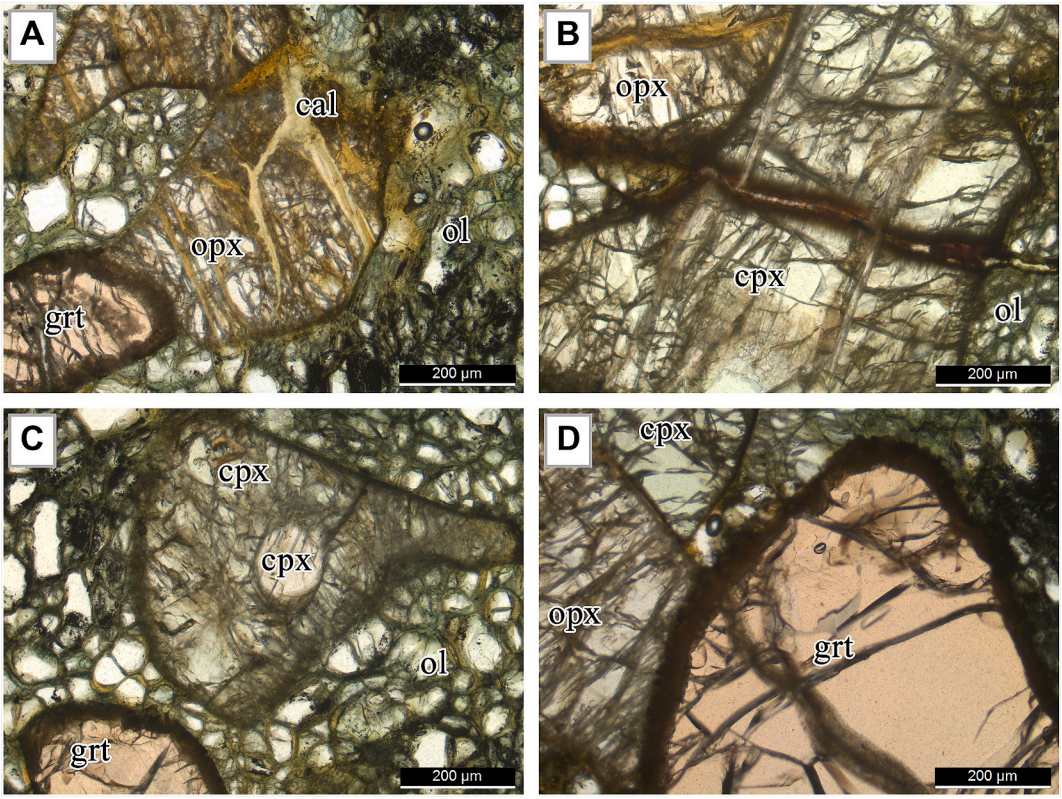

Fig. 3. Photomicrographs of minerals and textures observed in the Delitzsch sheared peridotite. *A: Orthopyroxene (opx) grain with veins following the cleavage planes. B:* Veined clinopyroxene (cpx) with reaction rim. C: Cpx with round cpx inclusion. D: *Large garnet (grt) crystal shows a prominent dark rim.* All pictures were taken under plane-polarized light (PPL).

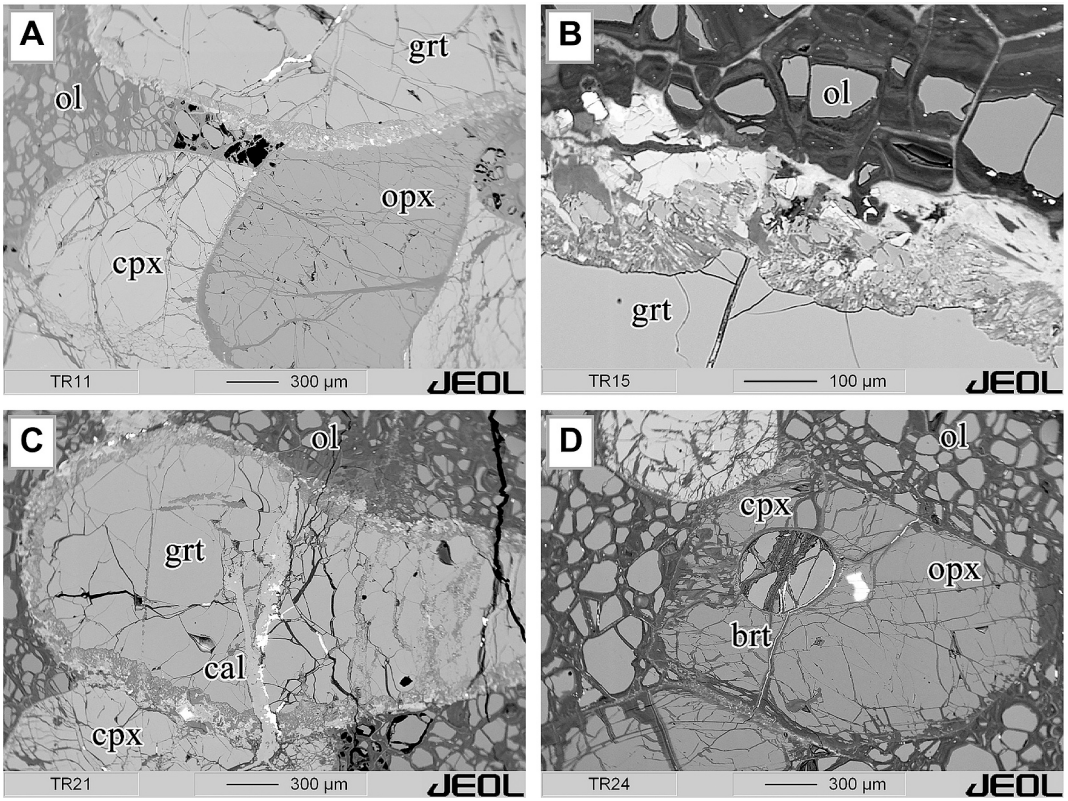

Fig. 4. BSE images of the Delitzsch sheared peridotite. *A: All four main phases are visible- garnet (grt) (top), orthopyroxene (opx) (darker phase, bottom center), clinopyroxene (cpx) (brighter phase, bottom left), and olivine (ol) (small crystals, left). B: close-up of a reaction rim around grt. C: Grt with calcite (cal) vein (bottom) and metasomatized ol (top). D: Cpx inclusion in opx with baryte (brt) vein. The bright patch in D represents local charging from the electron beam.*

olivine grains display the same gray tone in BSE imaging, indicating a similar composition and consistent Mg/Fe ratio. BSE images also provide a clear distinction between the extent of alteration observed in ortho- and clinopyroxene: orthopyroxene exhibits more extensive and larger veins as well as thicker reaction rims (Fig. 4A and Fig. 4D). EDS analysis shows that the presumed sulfate veins are baryte. Similar to the clinopyroxene-in-clinopyroxene inclusion described in Fig. 3C, a clinopyroxene-in-orthopyroxene inclusion is also observed (Fig. 4D). The kelyphite rims surrounding garnets (Fig. 4B) are primarily composed of secondary minerals such as amphiboles, pyroxenes, and spinel. Other minerals may be present, but could not be identified as grain sizes were too small to be resolved with EDS. The vein present within the garnet in Fig. 4C was identified as calcite.

Additionally, a rare potassium-rich sulfide was detected between olivine neoblasts in the groundmass. This sulfide was tentatively identified as rasvumite and is similar to that reported by Clarke et al. (1977) in a nodule from the Frank Smith kimberlite diatremes.

Except for groundmass olivine, no signs of significant alteration are discernable, and veins or reaction rims are observed mainly along fractures or around grain boundaries. Thus, the overall freshness of the sample is good and well-suited for in situ measurements.

4.2. Mineral chemistry data

A total of 174 points were measured on olivine, orthopyroxene, clinopyroxene and garnet. For clinopyroxene and garnet, both core and rim regions were analyzed separately (Table 1). Mean values, standard deviations (SD) and relative standard deviations (RSD) were calculated for each element in all minerals. The SD was further used as the uncertainty for the different oxide contents. All grains of the same phase only show minimal variation, i.e. below measurement uncertainty for all major elements and most trace elements. The average composition of the individual phases is given in Table 1 and shown in the major and trace element plots (Figs. 5, 6, 7, 9). The full EPMA dataset is available in the supplementary data (Table S2). Furthermore, the average of all measured grains for each mineral was used to calculate the molar fractions of each element for each respective mineral (Table 2). Oxide sums and cation sums deviate by less than 2 % from the expected values. For clinopyroxene and garnet, the mean of the measured core regions was used for plots, given that no internal zoning was observed and that the element variations in the rim can be attributed to later metasomatism or secondary alteration.

The data obtained for the Delitzsch sheared peridotite are compared to data for peridotites from a variety of studies, from different settings and origins. Garnet peridotite samples from the Saxothuringian Zone (Medaris et al., 2015), the Bohemian Massif (Medaris et al., 2005), the Ore Mountains (Schmädicke and Evans, 1997), and the Moldanubian Zone (Medaris et al., 2012; Muriuki et al., 2020) were chosen as comparison for local peridotite massifs. A group of deep-sourced (sheared) garnet peridotites of cratonic origin were chosen from the Slave Craton in Canada (Mather, 2012), the Kaapvaal Craton in South Africa (Heckel et al., 2022) and Lesotho (Heckel et al., 2023), from the São Francisco Craton in Brazil (Braga et al., 2024) as well as from two studies on sheared peridotites from Arkhangelsk Oblast in Russia (Kargin et al., 2021, 2017). Studies on plume-related spinel peridotites were chosen to compare against non-sheared peridotites, namely from the Eifel Volcanic Field in Germany (Witt-Eickschen and Kramm, 1998) and from the North China Craton (Cao et al., 2023). This last group also includes mantle xenoliths from basalts of the Kozákov Volcano in the Czech Republic (Ackerman et al., 2007). Data for the Primitive Mantle (PRIMA) were taken from (McDonough and Rudnick, 1998).

4.2.1. Olivine

The olivine neoblasts show a homogeneous composition for all

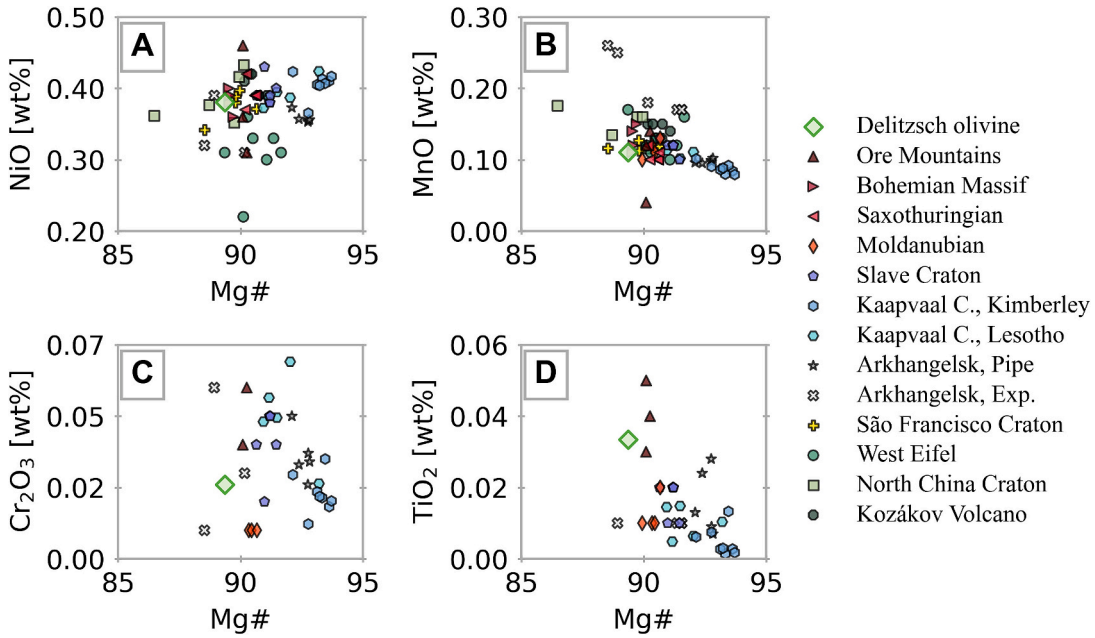

Fig. 5. Bivariate plots for olivine. A: NiO vs Mg#. B: MnO vs Mg#. C: Cr_2O_3 vs Mg#. D: TiO_2 vs Mg#. Means for ol data of the Delitzsch sheared peridotite plotted alongside grouped literature data (Ackerman et al., 2007; Braga et al., 2024; Cao et al., 2023; Heckel et al., 2023, 2022; Kargin et al., 2021, 2017; Mather, 2012; Medaris et al., 2015, 2012, 2005; Muriuki et al., 2020; Schmädicke and Evans, 1997; Witt-Eickschen and Kramm, 1998).

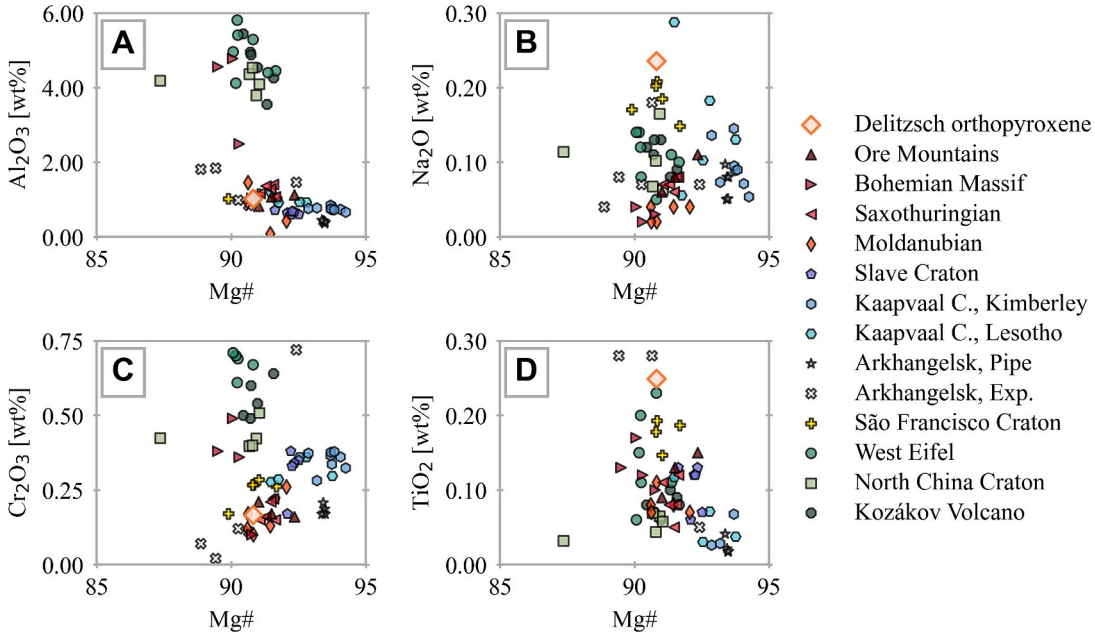

Fig. 6. Bivariate plots for orthopyroxene. A: TiO_2 vs Mg#. B: Al_2O_3 vs Mg#. C: Cr_2O_3 vs Mg#. D: Na_2O vs Mg#. Means for orthopyroxene data plotted alongside grouped literature data (Ackerman et al., 2007; Braga et al., 2024; Cao et al., 2023; Heckel et al., 2023, 2022; Kargin et al., 2021, 2017; Mather, 2012; Medaris et al., 2015, 2012, 2005; Muriuki et al., 2020; Schmädicke and Evans, 1997; Witt-Eickschen and Kramm, 1998).

measured grains (Table 1). Major element contents are tightly grouped with FeO (10.33 ± 0.13 wt%), MgO (48.70 ± 0.28 wt%), MnO (0.11 ± 0.02 wt%), and NiO (0.38 ± 0.01 wt%), resulting in a Mg# of 89.4 ± 0.1. The contents of minor elements display a wider relative distribution, including CaO (0.05 ± 0.01 wt%), TiO_2 (0.03 ± 0.01 wt%), and Cr_2O_3 (0.03 ± 0.01 wt%). Overall, the olivine solid solution can be classified as predominantly forsterite, with the formula $(Mg_{0.89}Fe_{0.11})_2SiO_4$.

Bivariate plots of our olivine data and literature data (Fig. 5) show that the Mg# is closer to PRIMA, i.e. 89.3 ((McDonough and Rudnick, 1998) than to those of the literature peridotites. Olivine from the Bohemian Massif (Medaris et al., 2005) show the closest match in major elements (Fig. 5A and B). The olivine from São Francisco craton sheared peridotites show strong overlap in Mg# as well as in the minor elements NiO and MnO (with no Cr_2O_3 or TiO_2 EPMA data available) (Braga et al., 2024). In contrast, other similarly textured cratonic samples (i.e., other sheared peridotites) have a more depleted Mg#, reaching up to 93.7 (Heckel et al., 2023, 2022; Mather, 2012). The contents of NiO and MnO resemble both cratonic samples and samples from local peridotite massifs but differ from plume-related peridotites. The Cr_2O_3 content

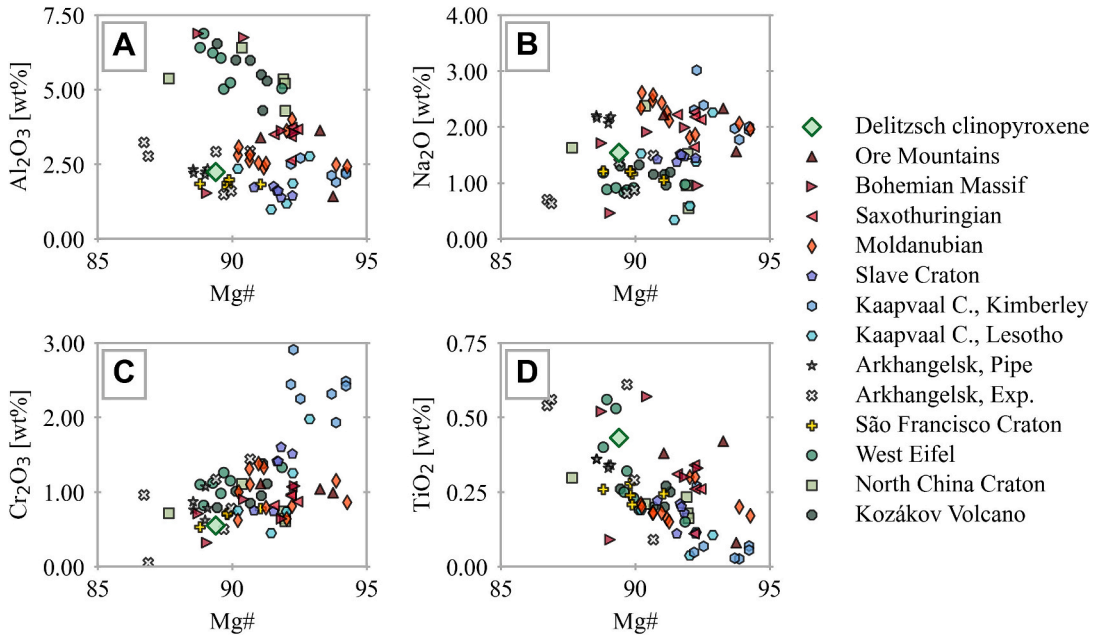

Fig. 7. Bivariate plots for clinopyroxene. A: TiO_2 vs Mg#. B: Al_2O_3 vs Mg#. C: Cr_2O_3 vs Mg#. D: Na_2O vs Mg#. Means of core regions for clinopyroxene data plotted alongside grouped literature data (Ackerman et al., 2007; Braga et al., 2024; Cao et al., 2023; Heckel et al., 2023, 2022; Kargin et al., 2021, 2017; Mather, 2012; Medaris et al., 2015, 2012, 2005; Muriuki et al., 2020; Schmädicke and Evans, 1997; Witt-Eickschen and Kramm, 1998).

Table 1
Representative composition (EPMA) of minerals in the Delitzsch sheared peridotite for olivine (ol), clinopyroxene (cpx), orthopyroxene (opx), and garnet (grt).

Minerals		Oxides [wt%]											
mean, SD and RSD		Na_2O	CaO	Al_2O_3	FeO	SiO_2	K_2O	MgO	TiO_2	Cr_2O_3	MnO	NiO	Sum
ol	mean	0.02	0.05	0.03	10.33	39.69	0.00	48.70	0.03	0.03	0.11	0.38	99.37
	sd	0.03	0.01	0.01	0.13	0.30	0.00	0.28	0.01	0.01	0.02	0.01	0.64
	rsd [%]	125	14	55	1.2	0.8	164	0.6	41	25	15	2.9	0.6
opx	mean	0.24	1.16	1.03	6.24	57.34	0.00	34.63	0.25	0.17	0.12	0.13	101.28
	sd	0.03	0.02	0.02	0.09	0.40	0.00	0.19	0.02	0.01	0.01	0.01	0.55
	rsd [%]	14	1.6	2.3	1.4	0.7	162	0.5	6.2	5.8	10	6.6	0.5
cpx core	mean	1.54	16.24	2.24	4.13	55.16	0.04	19.49	0.43	0.55	0.12	0.07	100.01
	sd	0.06	0.14	0.03	0.06	0.35	0.01	0.15	0.02	0.02	0.02	0.01	0.58
	rsd [%]	3.6	0.9	1.2	1.5	0.6	25	0.8	4.1	2.7	15	14	0.6
cpx rim	mean	0.99	18.12	1.43	4.19	54.59	0.03	19.54	0.60	0.58	0.12	0.06	100.26
	sd	0.30	1.56	0.45	0.31	0.80	0.04	0.65	0.18	0.05	0.02	0.01	0.98
	rsd [%]	31	8.6	32	7.4	1.5	135	3.3	30	7.8	16	18	1.0
cpx total	mean	1.42	16.67	2.06	4.14	55.03	0.04	19.50	0.47	0.56	0.12	0.06	100.06
	sd	0.28	1.08	0.41	0.15	0.54	0.02	0.33	0.11	0.03	0.02	0.01	0.69
	rsd [%]	20	6.5	20	3.7	1.0	53	1.7	24	5.0	15	15	0.7
grt core	mean	0.06	4.41	21.52	8.03	41.42	0.00	21.38	0.79	1.72	0.26	0.01	99.61
	sd	0.03	0.11	0.23	0.13	0.28	0.01	0.12	0.16	0.06	0.02	0.01	0.49
	rsd [%]	50	2.4	1.1	1.6	0.7	123	0.5	20	3.4	7.2	69	0.5
grt rim	mean	0.08	4.59	21.25	8.16	41.36	0.00	21.25	0.99	1.71	0.26	0.01	99.66
	sd	0.03	0.07	0.23	0.08	0.31	0.00	0.16	0.05	0.03	0.02	0.01	0.56
	rsd [%]	41	1.5	1	0.9	0.8	154	0.8	5.5	1.7	6.5	65	0.6
grt bulk	mean	0.07	4.50	21.39	8.09	41.39	0.00	21.32	0.89	1.71	0.26	0.01	99.63
	sd	0.03	0.13	0.27	0.12	0.29	0.01	0.15	0.16	0.05	0.02	0.01	0.52
	rsd [%]	46	2.8	1.2	1.5	0.7	138	0.7	18	2.7	7.0	67	0.5

plots close to the cratonic literature data, whereas the TiO_2 content is notably higher, closer to Ore Mountain peridotites (Fig. 5C and D).

4.2.2. *Orthopyroxene*

The orthopyroxene porphyroclasts show no evidence of chemical zoning with very little variation across all grains (Table 1). The mean values and standard deviations obtained are: FeO (6.24 ± 0.09 wt%), MgO (34.63 ± 0.19 wt%), MnO (0.12 ± 0.01 wt%), NiO (0.13 ± 0.01 wt %), Na_2O (0.24 ± 0.03 wt%), CaO (1.16 ± 0.02 wt%), Al_2O_3 (1.03 ± 0.02 wt%), TiO_2 (0.25 ± 0.02 wt%), and Cr_2O_3 (0.17 ± 0.01 wt%). The average Mg# was determined as 90.8 ± 0.1. The oxides were used to calculate the chemical formula $(Mg_{0.88}Fe_{0.09}Ca_{0.02})_2Si_2O_6$, classifying this opx as 88 % enstatite and 9 % ferrosilite, with a smaller fraction of wollastonite (Fig. S1).

In terms of Al_2O_3 and Cr_2O_3 contents, the Delitzsch orthopyroxene is similar to most orthopyroxene from local peridotite massifs (Fig. 6A and C), while Na_2O and TiO_2 contents plot significantly higher (Fig. 6B and D). The closest similarities for Na_2O and TiO_2 contents are found in sheared peridotites from the São Francisco Craton (Braga et al., 2024). Sheared peridotites from Lesotho (Heckel et al., 2023) show the closest match in Al_2O_3 contents, with other cratonic-sourced orthopyroxene having slightly lower Al_2O_3 contents. São Francisco Craton sheared

Table 2
Calculated molar fractions of minerals in the Delitzsch sheared peridotite for olivine (ol), clinopyroxene (cpx), orthopyroxene (opx), and garnet (grt).

Minerals	Molar fraction													SD
Averages	Si	Ti	Al	Cr	Fe	Mn	Mg	Ni	Ca	Na	K	Sum	Mg#	Mg#
ol	0.98	0.00	0.00	0.00	0.21	0.00	1.80	0.01	0.00	0.00	< LOD	3.02	89.4	0.1
opx	1.96	0.01	0.04	0.00	0.18	0.00	1.76	0.01	0.04	0.02	< LOD	4.02	90.8	0.1
cpx core	1.98	0.01	0.09	0.02	0.12	0.00	1.04	0.00	0.62	0.11	< LOD	4.01	89.4	0.1
cpx rim	1.97	0.02	0.06	0.02	0.13	0.00	1.05	0.00	0.70	0.07	< LOD	4.01	89.3	0.4
grt core	2.96	0.04	1.81	0.10	0.48	0.02	2.28	0.00	0.34	0.01	< LOD	8.04	82.6	0.2
grt rim	2.96	0.05	1.79	0.10	0.49	0.02	2.27	0.00	0.35	0.01	< LOD	8.04	82.3	0.2

peridotites exhibit very similar Mg# in opx. The plume-related spinel peridotites (Cao et al., 2023; Witt-Eickschen and Kramm, 1998), as well as the garnet peridotites from the Saxothuringian (Medaris et al., 2015) and Bohemian Massif (Medaris et al., 2005) also have similar Mg# values, while other cratonic literature data show a higher Mg# in orthopyroxene.

4.2.3. Clinopyroxene

For EPMA measurements of clinopyroxene the fresh core and the altered rim regions were examined (Table 1). The contents of FeO (4.13 ± 0.06 wt% core, 4.19 ± 0.31 wt% rim), MgO (19.49 ± 0.15 wt% core, 19.54 ± 0.65 wt% rim), MnO (0.12 ± 0.02 wt% core, 0.12 ± 0.02 wt% rim), NiO (0.07 ± 0.01 wt% core, 0.06 ± 0.01 wt% rim), and Cr_2O_3 (0.55 ± 0.02 wt% core, 0.58 ± 0.05 rim) remain very consistent between rims and cores. A Mg# of 89.4 ± 0.1 was calculated for the cores, and a value of 89.3 ± 0.4 for the rims. The contents of CaO (16.2 ± 0.1 wt% core, 18.1 ± 1.6 wt% rim), and TiO_2 (0.43 ± 0.02 wt% core, 0.60 ± 0.18 wt% rim) are higher in the rim region, whereas Na_2O (1.54 ± 0.06 wt% core, 0.99 ± 0.30 wt% rim), Al_2O_3 (2.24 ± 0.03 wt% core, 1.43 ± 0.45 wt% rim), are lower in the measured rims compared to the cores. A larger standard deviation was observed in the rim for all elements. When considering only core measurements, the chemical formula averages to $(Mg_{0.88}Fe_{0.09}Ca_{0.02}Na_{0.01})_2Si_2O_6$, identifying the clinopyroxene as an enstatite-rich augite (Fig. S1).

According to Ramsay's, 1992 classification, the Delitzsch clinopyroxene falls within the "on-craton" field (Fig. S2), near the "eclogites, pyroxenites and phenocrysts" group. The clinopyroxene compositions for most local peridotite massif peridotites plot in the same field. In contrast, despite the previously noted similar Mg#, plume-related spinel peridotites plot clearly within the "off-craton" field, reflecting the different setting.

The Delitzsch clinopyroxene exhibits a similar Al_2O_3, Na_2O and Cr_2O_3 content compared to clinopyroxenes found in sheared peridotites from the São Francisco Craton (Braga et al., 2024) and Slave Craton (Mather, 2012) (Fig. 7A, B, C). However, the TiO_2 contents (Fig. 7D) show no clear correlation, with the literature data displaying a wider range. Furthermore, only the spinel peridotites from the Eifel (Witt-Eickschen and Kramm, 1998) and sheared peridotites from São Francisco Craton (Braga et al., 2024) show a comparable Mg#. The closest overall resemblance is found in the peridotites from the São Francisco Craton, which have slightly lower TiO_2 contents (Fig. 7D).

4.2.4. Garnet

EPMA measurements on garnets were also separated into cores and rims (Table 1). The rim measurements were taken within the porphyroclasts near their grain boundaries, but not in the altered kelyphite regions. In contrast to clinopyroxene, garnet grains show no significant change in composition between the two regions. The average contents and standard deviations are as follows: FeO (8.03 ± 0.13 wt%), MgO (21.38 ± 0.12 wt%), MnO (0.26 ± 0.02 wt%), Na_2O (0.06 ± 0.03 wt%), CaO (4.41 ± 0.11 wt%), Al_2O_3 (21.52 ± 0.23 wt%), TiO_2 (0.79 ± 016 wt %), and Cr_2O_3 (1.72 ± 0.06 wt%). Only Na_2O (0.08 ± 0.03 wt%) and TiO_2 (0.99 ± 0.06 wt%) showed a slight increase towards the rim. The Mg# of the cores is 82.6 ± 0.2 and 82.3 ± 0.2 for rims. Calculation of molar fractions result in a chemical formula of $(Ca_{0.11}Mg_{0.76}Fe_{0.16})_3(Al_{0.91}Cr_{0.05})_2Si_3O_{12}$, classifying the garnet as mostly pyrope with nearly equal parts of almandine and grossular.

Adding the measured data to the garnet classification plot of Grütter et al. (2004) (Fig. 8) requires careful consideration and interpretation. At first glance, the Delitzsch garnets compositions appears to lie within field G5 for "pyroxenitic, websteritic and eclogitic" garnet. However, Grütter et al. (2004) also provide a sequence for testing compositional compliance as follows: G1-G11-G10-G19-G12-G5-G4-G3-G0, and they specify additional criteria for classification. For G1, coarse-grained garnets (2-10 cm) are mentioned, while G11 specifically includes sheared peridotites. To fit within G11, garnets must meet the following criteria: Cr_2O_3 between 1.0 and 20.0 wt% (this study: 1.71 wt%), CaO less than 28.0 wt% (this study: 4.41 wt%), Mg# between 65 and 90 (this study: 82.6), and TiO_2 less than 4 wt% (this study 0.79 wt%) but also equal or greater than 2.13-2.1 × Mg# (this study requires >0.395). Additionally, CA_INT (here calculated as CaO-0.25 × Cr_2O_3) must be above three (this study: 3.99). With all these requirements fulfilled, the Delitzsch garnet can be classified as a G11-type "high-TiO_2 peridotitic" garnet. Considering the above limitations by Grütter et al. (2004), local massif peridotites plot within the G5 group, whereas sheared peridotites from São Francisco Craton (Braga et al., 2024) are the only G11 group samples that plot in proximity to our sample.

Bivariate plots for garnet (Fig. 9) place the Mg# midway between samples from the Saxothuringian Zone (Medaris et al., 2015) and those from the Slave Craton (Mather, 2012). The contents of Al_2O_3 and the Cr# (Cr/[Cr + Al] × 100) align well with the local massif peridotites (Fig. 9A and C, respectively), whereas MnO contents most closely resemble those of the Kaapvaal Craton samples from Lesotho (Heckel et al., 2023). The measured TiO_2 contents plot close to the Slave Craton samples. Again, the compositions are most similar to those in sheared peridotites from the São Francisco craton (Braga et al., 2024).

4.3. LA-ICP-MS data

Where possible, trace element analyses were performed on the same grains previously measured by EPMA. The concentrations were homogeneous for each mineral, allowing the results to be averaged (Table 3). In Table 4, trace element abundances are provided normalized to CI-chondrite composition (Palme and O'Neill, 2014). The full LA-ICP-MS dataset is available in the supplementary data (Table S3).

For olivine, trace element concentrations of Sr, Ce and Pb are excluded as they are below the LOD. All other olivine data fall within a 2 SD range of less than 10 %, with the exception of Y and Nb, due to their low concentrations. Four measured spots on olivine were excluded due to anomalous data, possibly caused by the beam hitting impurities or other grains. Three excluded spots (all in the same grain) exhibited Al concentration that were double to triple the mean concentration observed in olivine, which could be due to minute spinel inclusions (see below). Another grain showed very high signals for Ca and Sr, likely

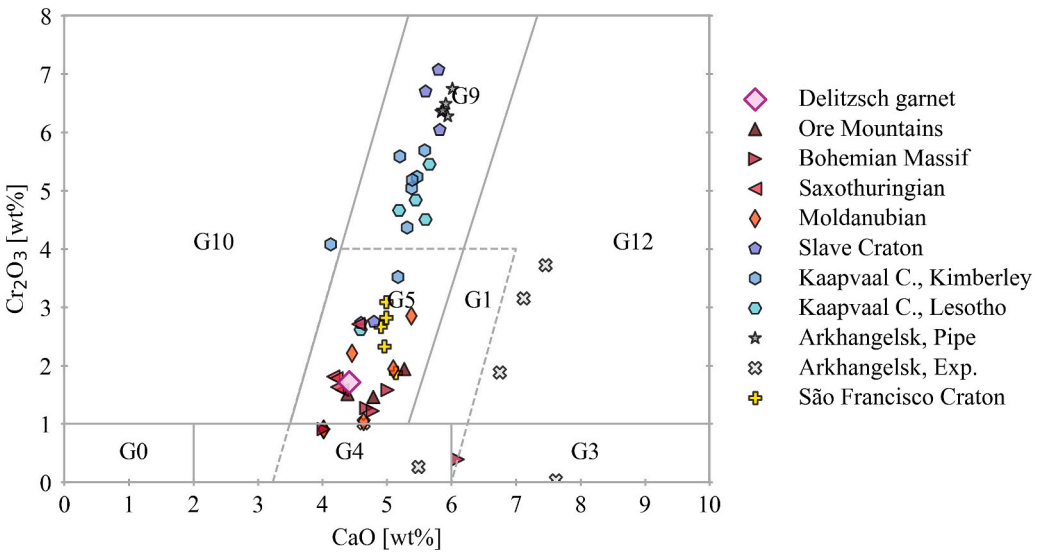

Fig. 8. Garnet classification plot (after Grütter et al., 2004). Means of core regions for garnet data plotted alongside grouped literature data (Braga et al., 2024; Heckel et al., 2023, 2022; Kargin et al., 2021, 2017; Mather, 2012; Medaris et al., 2015, 2012, 2005; Muriuki et al., 2020; Schmädicke and Evans, 1997). The fields represent groups of different origin or setting:"G10" harzburgitic; "G9" lherzolitic; "G12" wherlitic; "G1" low-Cr megacrysts; "G4" and"G5" pyroxenitic, websteritic and, eclogitic; "G3" eclogitic; "G0" unclassified. "G11" high-TiO_2 peridotitic must be classified separately.

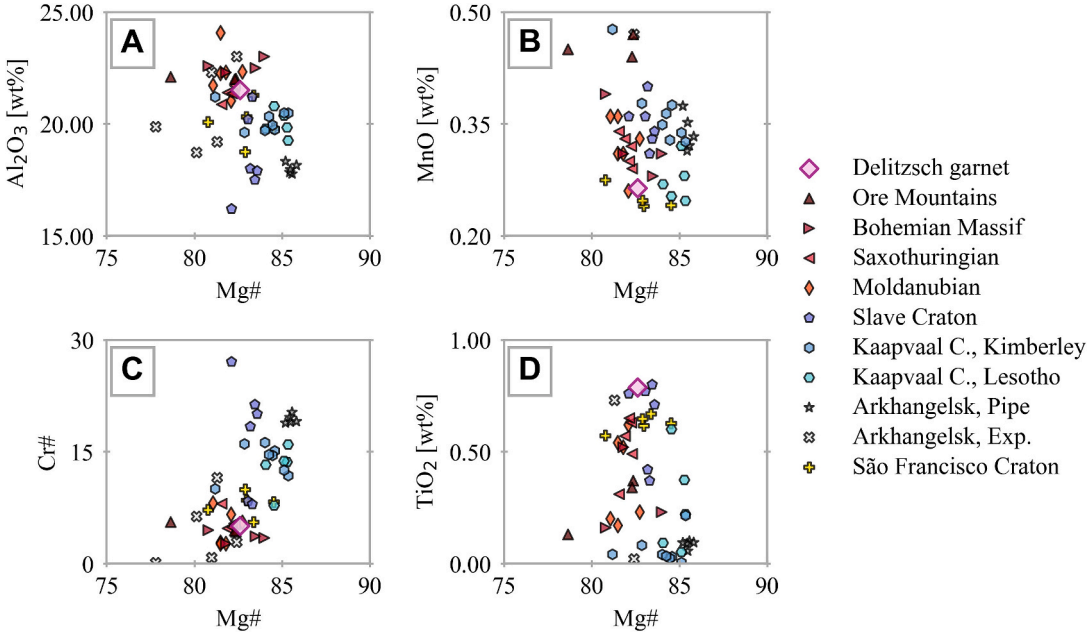

Fig. 9. Bivariate plots of element data for garnet. A: TiO_2 vs Mg#. B: Al_2O_3 vs Mg#. C: Cr_2O_3 vs Mg#. D: Na_2O vs Mg#. Means of core regions for garnet data of the Delitzsch sheared peridotite plotted alongside grouped literature data (Braga et al., 2024; Heckel et al., 2023, 2022; Kargin et al., 2021, 2017; Mather, 2012; Medaris et al., 2015, 2012, 2005; Muriuki et al., 2020; Schmädicke and Evans, 1997).

indicating the presence of a carbonate vein.

For both ortho- and clinopyroxene, Rb must be evaluated carefully, as some grains had concentrations below the LOD, resulting in higher uncertainty. The Ba concentration of one point in clinopyroxene had to be excluded due to anomalous high concentrations, likely caused by the laser hitting a baryte vein. Additionally, low concentrations of Pb, Th, and U in orthopyroxene lead to higher variance in the respective values.

Garnet data revealed four elements with concentrations below the LOD: K, Rb, Ba, and Pb. Higher variance was observed for Zr, Hf, Ta, Th, and U. For the latter four elements, this variance can be attributed to low concentrations, while the variance in Zr may be due to natural heterogeneities.

Based on the observed similarities in major element compositions, sheared peridotites from Lesotho (Heckel et al., 2023) and from the São Francisco Craton (Braga et al., 2024) were selected as the primary literature data for comparisons. Heckel et al. (2023) grouped sheared peridotites into three categories: Group I "Low-T sheared peridotites", Group II "Moderate-T sheared peridotites", and Group III "High-T sheared peridotites". These groups are based on temperature and depth determined during equilibration, as well as the enrichment or depletion of light rare earth elements (LREE), middle rare earth elements (MREE) and heavy rare earth elements (HREE). Metasomatic tracers such as Nb—Ta, Zr—Hf, and Ti are used as additional indicators. Heckel et al. (2023) base their groups on the work of Boyd and Nixon (1978), with

Table 3
Representative trace element concentrations (LA-ICP-MS) in the Delitzsch sheared peridotite for olivine (ol), clinopyroxene (cpx), orthopyroxene (opx), and garnet (grt).

Element	Mineral	Element	Mineral		
c [ppm]	ol	c [ppm]	opx	cpx	grt
Li	1.99	Na	1810	11,700	538
Na	173	K	4.34	347	< LOD
Al	151	Ca	7850	116,000	26,800
Ca	409	Sc	8.14	15.9	60.2
Ti	171	Ti	1330	2340	3710
V	10.0	V	55.7	208	210
Cr	156	Ni	999	560	114
Mn	825	Zn	49.2	21.9	18.9
Co	144	Rb	0.029	0.030	< LOD
Ni	2900	Sr	1.88	205	0.644
Cu	6.84	Y	0.178	2.89	14.4
Zn	79.7	Zr	0.652	11.0	53.4
Ga	0.255	Nb	0.050	0.217	0.194
Sr	< LOD	Ba	0.164	0.365	< LOD
Y	0.011	La	0.022	2.93	0.035
Zr	0.142	Ce	0.107	11.24	0.40
Nb	0.0179	Pr	0.0201	1.94	0.148
Ce	< LOD	Nd	0.132	9.64	1.408
Pb	< LOD	Sm	0.0436	2.10	1.050
		Eu	0.0157	0.628	0.485
		Gd	0.0468	1.56	1.65
		Tb	0.0067	0.181	0.327
		Dy	0.0395	0.816	2.36
		Ho	0.0067	0.122	0.550
		Er	0.0170	0.2566	1.72
		Tm	0.0027	0.0266	0.257
		Yb	0.0121	0.1403	1.91
		Lu	0.0015	0.0161	0.291
		Hf	0.0329	0.6165	1.23
		Ta	0.0036	0.0123	0.0141
		Pb	0.0041	0.163	< LOD
		Th	0.0010	0.0229	0.0053
		U	0.0007	0.0042	0.0086

Table 4
Trace element concentrations (LA-ICP-MS) normalized to CI for olivine (ol), clinopyroxene (cpx), orthopyroxene (opx), and garnet (grt).

Element	Mineral	Element	Mineral		
	ol		opx	cpx	grt
Li	1.33	Na	0.36	2.3	0.11
Na	0.034	K	0.0079	0.63	< LOD
Al	0.018	Ca	0.22	3.3	0.77
Ca	0.012	Sc	1.4	2.7	10
Ti	0.39	Ti	3.0	5.3	8.4
V	0.18	V	0.99	3.7	3.7
Cr	0.059	Ni	0.095	0.053	0.011
Mn	0.31	Zn	0.16	0.071	0.061
Co	0.075	Rb	0.013	0.013	< LOD
Ni	5.80	Sr	0.26	28	0.089
Cu	< LOD	Y	0.11	1.8	9.2
Zn	0.26	Zr	0.17	2.9	14
Ga	0.028	Nb	0.21	0.90	0.81
Sr	< LOD	Ba	0.068	0.15	< LOD
Y	0.007	La	0.092	12	0.15
Zr	0.037	Ce	0.17	18	0.66
Nb	0.075	Pr	0.22	21	1.6
Ce	< LOD	Nd	0.29	21	3.1
Pb	< LOD	Sm	0.29	14	7.1
		Eu	0.28	11	8.6
		Gd	0.24	7.8	8.3
		Tb	0.18	5.0	9.1
		Dy	0.16	3.3	9.6
		Ho	0.12	2.2	10
		Er	0.11	1.6	11
		Tm	0.11	1.1	10
		Yb	0.075	0.9	12
		Lu	0.062	0.7	12
		Hf	0.32	6.0	12
		Ta	0.26	0.90	1.0
		Pb	0.002	0.066	< LOD
		Th	0.036	0.79	0.18
		U	0.098	0.57	1.2

Groups II and III belonging to the suite of high-T sheared peridotites. High-T peridotites are defined by an equilibration temperature above 1100 °C, while Group I peridotites are equilibrated below 1100 °C accordingly.

4.3.1. Olivine

Where possible, the LA-ICP-MS results were directly compared to the respective EPMA data. For this purpose, all relevant oxide contents were calculated from concentrations obtained via LA-ICP-MS. The measured contents of MnO and NiO are in good agreement (i.e., within 5 %) for both methods, as well as with the corresponding standard for each method (Table S4), allowing these values to be used with high confidence. However, oxides with low abundance, such as Na_2O, Al_2O_3, and Cr_2O_3, show significantly higher contents when calculated from LA-ICP-MS data. Oxide data measured by EPMA close to their respective LODs inherently have lower accuracy; in these cases, the LA-ICP-MS data are preferred. This adjustment would result in a slight increase in the Cr_2O_3 content shown in Fig. 5C. The calculated TiO_2 content could potentially be slightly corrected to lower levels, as deviations of 10 % or more can be considered significant.

When plotting the Delitzsch trace element results for olivine in classification diagrams for peridotites (Bussweiler et al., 2017; De Hoog et al., 2010) the data clearly lies in the garnet peridotite field (Fig. 10). This further highlights the good compositional equilibrium, in major and trace elements, among the different minerals.

4.3.2. Orthopyroxene

The trace element patterns for orthopyroxene reveal sub-chondritic concentrations for all elements (Fig. 11), except for a pronounced positive Ti anomaly (~5× chondritic). Incompatible trace elements such as Rb, Ba, Th and U are depleted matching Group II and III sheared peridotites of Heckel et al. (2023). The pattern shows an increase from LREE towards MREE. A positive Nb—Ta anomaly is observed, while Zr exhibits a negative anomaly. Additionally, there is a decrease in concentrations from MREE to HREE.

The Delitzsch orthopyroxene shows the best overall overlap with the Group II sheared peridotites from Lesotho, while one Group III sample also has a similar pattern (Fig. 11). Notably, a slight positive Nb—Ta anomaly is observed, and the Ti concentration is exceptionally high in our study. Group I peridotites from Lesotho are less depleted in incompatible trace elements, except for some MREE, while Group III peridotites are generally more depleted in REE by more than one order of magnitude, with sample Let 9 of Heckel et al. (2023) being an exception.

4.3.3. Clinopyroxene

Clinopyroxene show a more enriched trace element pattern (Fig. 12) compared to orthopyroxene from the Delitzsch sheared peridotite. The trace elements Rb and Ba are highly depleted, with sub-chondritic values, followed by a steep increase towards Th then flattening until Nb and Ta, which approach chondritic values. LREE and Sr are enriched up to ~28× chondritic abundances. The concentrations decrease from the MREE towards the HREE, with Yb and Lu returning the pattern to sub-chondritic levels.

Trace element patterns in this study, particularly for LREE and MREE, closely resemble those of sample BD2171 from Lesotho, while the HREE show a close match to sample Let 9 of Heckel et al. (2023). General criteria for Group II and III peridotites in clinopyroxene-trace element plots include a flat Nb—Ta pattern and a negative Zr—Hf anomaly. Additionally, Group II exhibits a slightly negative Ti anomaly, which may be absent in Group III (Heckel et al., 2023). A further match

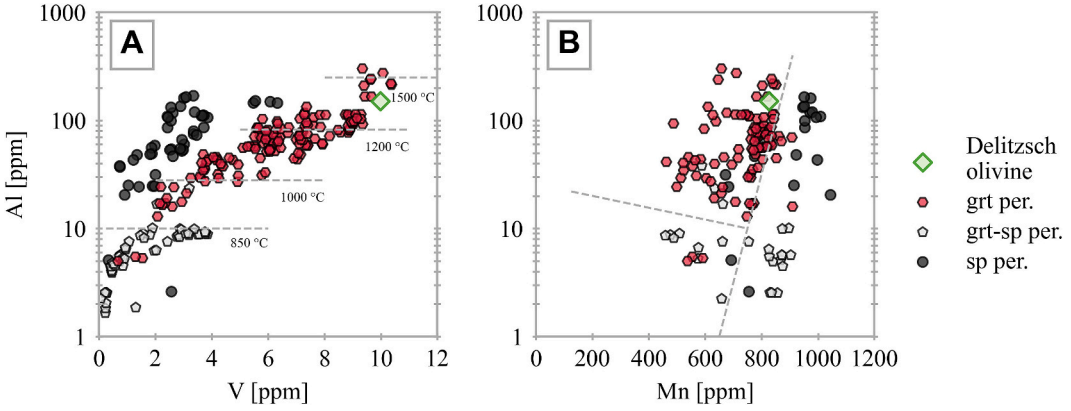

Fig. 10. Bivariate plots of trace element concentrations in olivine. A: Al (log) vs V, modified after Bussweiler et al., 2017. B: Al (log) vs Mn, modified after De Hoog et al., 2010. The different types of peridotites are grouped together respectively: garnet peridotites in red, garnet-spinel peridotites in white and spinel peridotites in black. Temperature contours in A are based on a geotherm of 40 mW/m^2. Literature data from various cratonic settings (Bussweiler et al., 2017; De Hoog et al., 2010 and references therein). (For interpretation of the references to colour in this figure legend, the reader is referred to the web version of this article.)

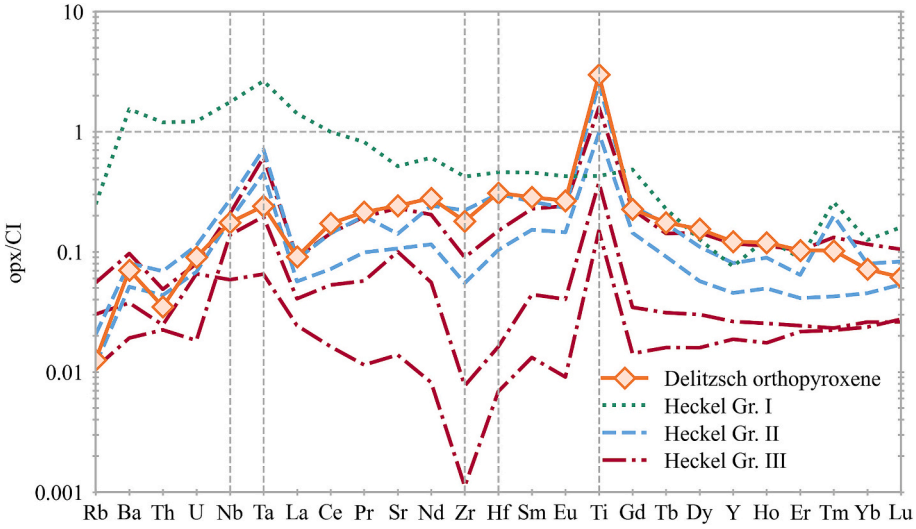

Fig. 11. Chondrite-normalized trace element diagram for orthopyroxene (CI-Chondrite from Palme and O'Neill (2014)). In light green: Group I "Low-T sheared peridotites". In blue: Group II "Moderate-T sheared peridotites". In red: Group III "High-T sheared peridotites". Grouped literature data and compositional garnet-peridotite groups from Heckel et al. (2023). (For interpretation of the references to colour in this figure legend, the reader is referred to the web version of this article.)

is found in the six São Francisco Craton peridotites (Braga et al., 2024). These samples are slightly more enriched in trace elements but show lower overall LREE and MREE compared to the Delitzsch clinopyroxene. In contrast, clinopyroxene in garnet peridotites from the Moldanubian Zone (Medaris et al., 2012) are clearly enriched in Th and U, which is a typical crustal signature (Fig. 12).

4.3.4. Garnet

For garnet, the normalized values were plotted in a REE diagram (Fig. 13). The garnets in this study display a steady increase from the LREEs, starting with La at 0.15× chondritic to Sm at 7× chondritic, followed by a slight but consistent increase through the MREEs and HREEs. Such patterns are described in the literature as a "normal" shape (e.g., Stachel et al., 1998). These "normal" or "L-shaped" patterns are characterized by a gradual increase from LREEs up to Sm, with this trend tapering off through the MREEs and HREEs. In contrast, harzburgitic garnets exhibit a "sinusoidal pattern," as shown in the Group I data in Fig. 13, characterized by an enrichment of LREEs and depletion of HREEs.

Literature data for Lesotho Group I (low-T) sheared peridotites and some Group II peridotites typically exhibit a sinusoidal shape, while garnets in Group III peridotites display a normal shape with potentially higher degrees of depletion (Heckel et al., 2023). The pattern observed in this study closely resembles that of sample Let 9 from Lesotho (Fig. 13). A comparison between the Delitzsch garnet and the São Francisco Craton garnets (Braga et al., 2024) reveals a very similar shape and concentration profile. While LREEs are more enriched in the São Francisco Craton samples, both curves begin to converge, with the Delitzsch garnet showing only slightly lower concentrations in MREEs and HREEs. In contrast, garnet in garnet peridotites from the Moldanubian Zone (Medaris et al., 2012) are significantly more depleted in LREE (Fig. 13).

4.4. Geothermobarometry

Thermobarometric calculations were performed using PTEXL, a spreadsheet provided by the diamond research group at the University of Alberta (Stachel, 2022). For major and minor elements, the EPMA data (core and rim analyses) were used, and for trace elements the LA-ICP-MS data were used in the calculations. PTEXL includes data

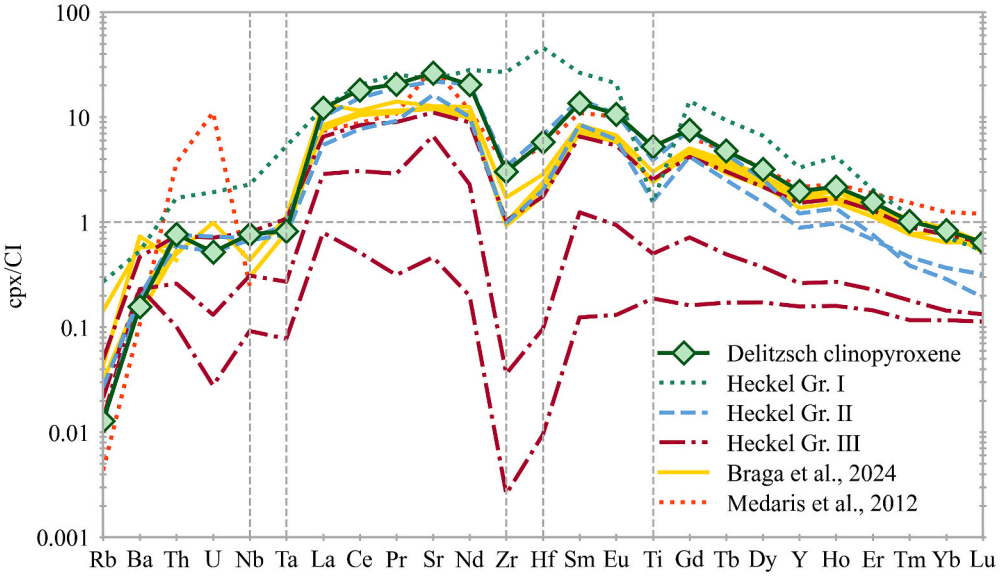

Fig. 12. Chondrite-normalized trace element diagram for clinopyroxene (CI-Chondrite from Palme and O'Neill (2014)). In light green: Group I "Low-T sheared peridotites". In blue: Group II "Moderate-T sheared peridotites". In red: Group III "High-T sheared peridotites". Grouped literature data and compositional garnet-peridotite groups from Heckel et al. (2023). In yellow: clinopyroxene from sheared peridotites from the São Francisco craton (Braga et al., 2024). In orange: clinopyroxene from the Sklené garnet peridotite from the Moldanubian Zone (Medaris et al., 2012). (For interpretation of the references to colour in this figure legend, the reader is referred to the web version of this article.)

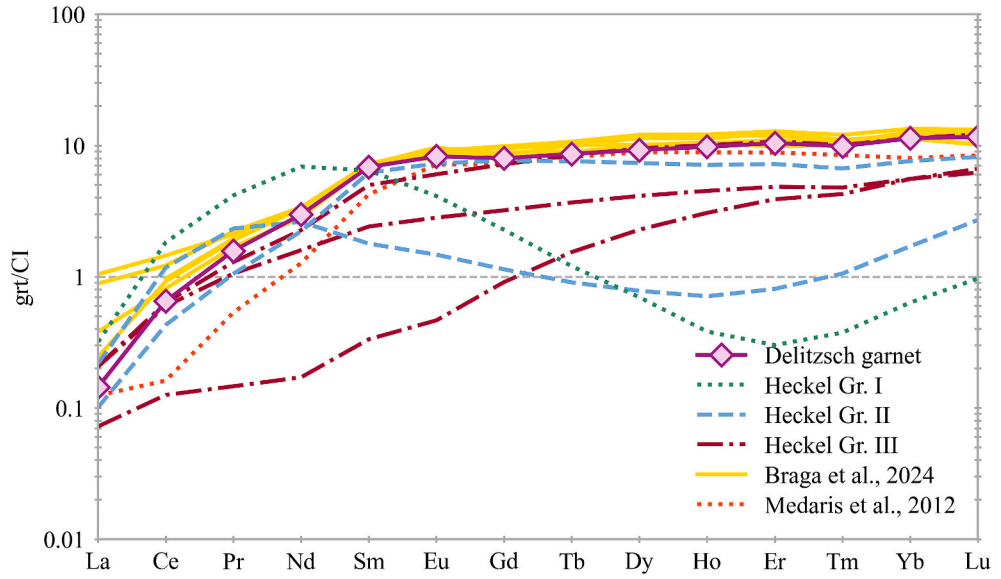

Fig. 13. Chondrite-normalized rare earth element diagram for garnet (CI-Chondrite from Palme and O'Neill (2014)). In light green: Group I "Low-T sheared peridotites". In blue: Group II "Moderate-T sheared peridotites". In red: Group III "High-T sheared peridotites". Grouped literature data and compositional garnet-peridotite groups from Heckel et al. (2023). In yellow: garnet from sheared peridotites from the São Francisco craton (Braga et al., 2024). In orange: garnet from the Sklené garnet peridotite from the Moldanubian Zone (Medaris et al., 2012). (For interpretation of the references to colour in this figure legend, the reader is referred to the web version of this article.)

quality assessments, such as oxide sum tests, as well as equilibrium checks to evaluate the results. Certain thermometers within PTEXL are tailored for garnet peridotites or require specific parageneses, requiring additional checks for rock composition. Equilibrium checks validated that the EPMA core measurements are representative of a system in equilibrium, whereas the rim data exhibited a slight divergence from the acceptable thresholds. Consequently, only EPMA core data were used for deducing the P-T conditions of equilibration of the Delitzsch sheared peridotite. To reinforce the accuracy of the results, various pairs of geothermometers and -barometers were applied iteratively (Table 5):

The two-pyroxene thermometer T_{BKN} was used in combination with the garnet-orthopyroxene barometer P_{BKN} (Brey and Köhler, 1990). Additionally, the garnet-clinopyroxene Fe—Mg thermometer $T_{Krogh88}$ (Krogh, 1988) and the Al-in-olivine thermometer $T_{Al\text{-}in\text{-}olivine}$ (Bussweiler et al., 2017) were also combined with P_{BKN}. The Cr-in-clinopyroxene thermometer T_{NT} was applied in various combinations with the enstatite-in-clinopyroxene barometer P_{NT} (Nimis and Taylor, 2000), the corrected barometer P_{NTcorr} (Nimis et al., 2020), and the Cr-in-clinopyroxene barometer P_{SUD} (Sudholz et al., 2022). The final iteratively solved combination consists of the two-pyroxene thermometer T_{TA} (Taylor and Nimis, 1998) and the garnet-orthopyroxene barometer P_{NG} (Nickel and Green, 1985).

Table 5
Summary of calculated pressures and temperatures. Clinopyroxene (cpx) and garnet (grt) cores and rims were calculated individually.

Iterative Methods	Sampling		
T [°C], P [kbar]	**bulk minerals**	**cpx, grt- core**	**cpx, grt- rim**
T [BKN/BKN]	1362	1374	1318
P [BKN/BKN]	60.4	61.0	57.5
T [NTcpx/NT-corrcpx]	1316	1323	1287
P [NT-corrcpx/NTcpx]	62.9	62.7	63.8
T [NTcpx/SUDcpx]	1329	1338	1296
P [SUDcpx/NTcpx]	68.5	68.8	67.6
T [Krogh88/BKN]	1304	1304	1311
P [BKN/Krogh88]	56.4	56.4	57.0
T [Al-in-olivine/BKN]	1310	1309	1310
P [BKN/Al-in-olivine]	56.8	56.7	57.0
Results after Nimis et al. (2024)			
P-dependent thermometer		**T for bulk minerals [°C]**	
$P_{assumed}$	58.0 kbar		1326
$P_{assumed}$	60.0 kbar		1334
P-indipendent, geotherm based thermometer			
$W_{assumed}$	40 mW/m^2		1339
$W_{assumed}$	45 mW/m^2		1263

Calculated pressures range from 56.4 kbar to 68.8 kbar, with an average of 61.1 kbar. This corresponds to a depth of 190 km (Hasterok and Chapman, 2011). These pressure estimates were used to apply the revised Ni-in-garnet geothermometer (Nimis et al., 2024), resulting in temperatures that range from 1263 °C to 1362 °C with an overall average of 1330 °C. Uncertainties based on the deviations between individual thermo- and barometers are ±23 °C and ± 5.1 kbar, respectively. It should be noted that thermometers based on major (e.g., garnet-clinopyroxene Fe—Mg) and trace elements (e.g., Ni-in-garnet, Al-in-ol) all provide consistent results.

Three representative geothermometer and -barometer combinations were plotted against respective results for literature data (Fig. 14). All combinations position the Delitzsch garnet peridotite within the diamond stability field. Two of these combinations place the sample near the asthenospheric adiabat, while the two-pyroxene thermometer and garnet-orthopyroxene barometer combination (Brey and Köhler, 1990) plots directly on the adiabat (Fig. 14A). Additionally, three geotherms for the continental lithosphere were included (Hasterok and Chapman, 2011). A geotherm corresponding to a heat flow of 40 mW/m^2, or slightly higher, appears to be the best fit to our data. Literature data from the São Francisco Craton in Brazil (Braga et al., 2024) and the Kaapvaal Craton in Lesotho (Heckel et al., 2023) show the most comparable P-T results, whereas the data for local peridotite massifs (Medaris et al., 2015, 2005; Schmädicke and Evans, 1997) and the Eifel literature data (Witt-Eickschen and Kramm, 1998) clearly lie at significantly lower P-T conditions.

5. Discussion

5.1. Reconstruction of whole-rock composition

In addition to the direct comparison of mineral compositions, whole-rock compositions allow for a more complete comparison with different mantle types (e.g., primitive mantle, on-/off-craton lithospheric mantle etc.). To reconstruct the whole-rock composition of the sheared garnet peridotite of this study, the modal proportions and the major and trace element data for each mineral were used. An estimated modal composition of 61 % olivine, 13 % clinopyroxene, 15 % orthopyroxene, and 11 % garnet (Table 6) was obtained through image analysis of the thick section scans, with corrections based on the specific densities of each mineral. The number of pixels representing each phase was calculated using Adobe Photoshop and averaged across both sections. The primary criterion for selection was the visibility of grain boundaries, as shown in Fig. 3. To determine the pixel area for olivine, the areas corresponding to orthopyroxene, clinopyroxene, and garnet were subtracted from the total sample area. Minerals found in veins or inclusions were excluded from the calculations. The size differences of individual grains between the two thick sections are likely due to the sections cutting through regions of varying crystal thickness during preparation. The significant variation in garnet grain sizes may impact the overall modal and bulk composition, potentially leading to an underestimation of the bulk Mg#. A similar analysis focusing solely on garnet was conducted on the frontal face of the original sample shown in Fig. 2, which reinforced the 10 % modal abundance estimate for garnet.

Based on the previously determined chemical formulas, specific densities (Johnson and Olhoeft, 1984) for the present solid solutions were estimated and then normalized to 100 %. Using the modal composition as a weight factor for the major element oxide contents, an overall bulk composition was calculated (Table 7). This method yields bulk MgO and FeO contents of 39.6 wt% and 8.6 wt%, respectively, resulting in a calculated Mg# of 89.1. The SiO_2 content is determined to be 44.6 wt%. The relatively high TiO bulk content of 0.2 wt% is noteworthy. McDonough and Rudnick (1998) provide reference compositions for various crustal and upper mantle lithologies. In a compositional spectrum ranging from primitive mantle (PRIMA) to increasingly depleted materials (e.g., dunite), the calculated whole-rock composition of this study is placed between PRIMA and off-craton lherzolites based on major element contents. Considering the uncertainties (cf. RSD in Table 1) in the bulk calculations, a fertile, lherzolitic source appears to be most likely.

5.2. Significance of the first sheared garnet peridotite mantle xenolith in Germany

The classification of the sample as a sheared garnet peridotite (lherzolite) is supported by its mineralogy, texture and chemical composition. Both the optical estimate and the calculated modal and bulk compositions confirm the sample as a lherzolitic garnet peridotite (McDonough and Rudnick, 1998). In contrast, other described peridotites from German localities are either spinel peridotites (cf. Fig. S2) or not lherzolitic in nature (cf. Fig. 8). The mosaic to slightly fluidal mosaic texture and elongated garnet grains as described in the Petrography section, is consistent with sheared peridotites from other locations worldwide (Braga et al., 2024; Heckel et al., 2022, 2023; Kargin et al., 2017).

Geothermobarometry yields equilibration conditions of around 61.1 kbar and 1330 °C, corresponding to a depth of around ~190 km. For comparison, all samples from local peridotite massifs, as well as peridotites from the Eifel region, indicate formation at both lower pressures (less than 40 kbar) and lower temperatures (below 1100 °C). Other studies focusing on microdiamond-bearing rocks from the Saxothuringian (Massonne, 1998) represented the deepest samples in Germany prior to this study, but they also fall short of 50 kbar. Thus, the analyzed sample not only represents the first sheared garnet lherzolite but also the deepest sample ever recorded from Germany. Furthermore, the xenolith could represent a non-cratonic sheared peridotite (Braga et al., 2024) or a lithospheric relic from the Bohemian Massif. These findings imply a) the existence of thick lithosphere during the Cretaceous and b) the consequent destruction of such thick lithosphere, as the present-day lithosphere is much thinner (see below).

5.3. Origin of deformation and reaction textures

The high pressure and high temperature regime of the sample can explain the sheared garnet grains and the slightly fluidal texture in the olivine matrix. A convecting, ductile asthenosphere would provide the shear strain necessary to deform garnet heated to the point of superplasticity. This process is believed to be related to the formation of fluidal textures in olivine (Harte, 1977). However, recent studies suggest that the ascent/emplacement process itself is cause for deformation

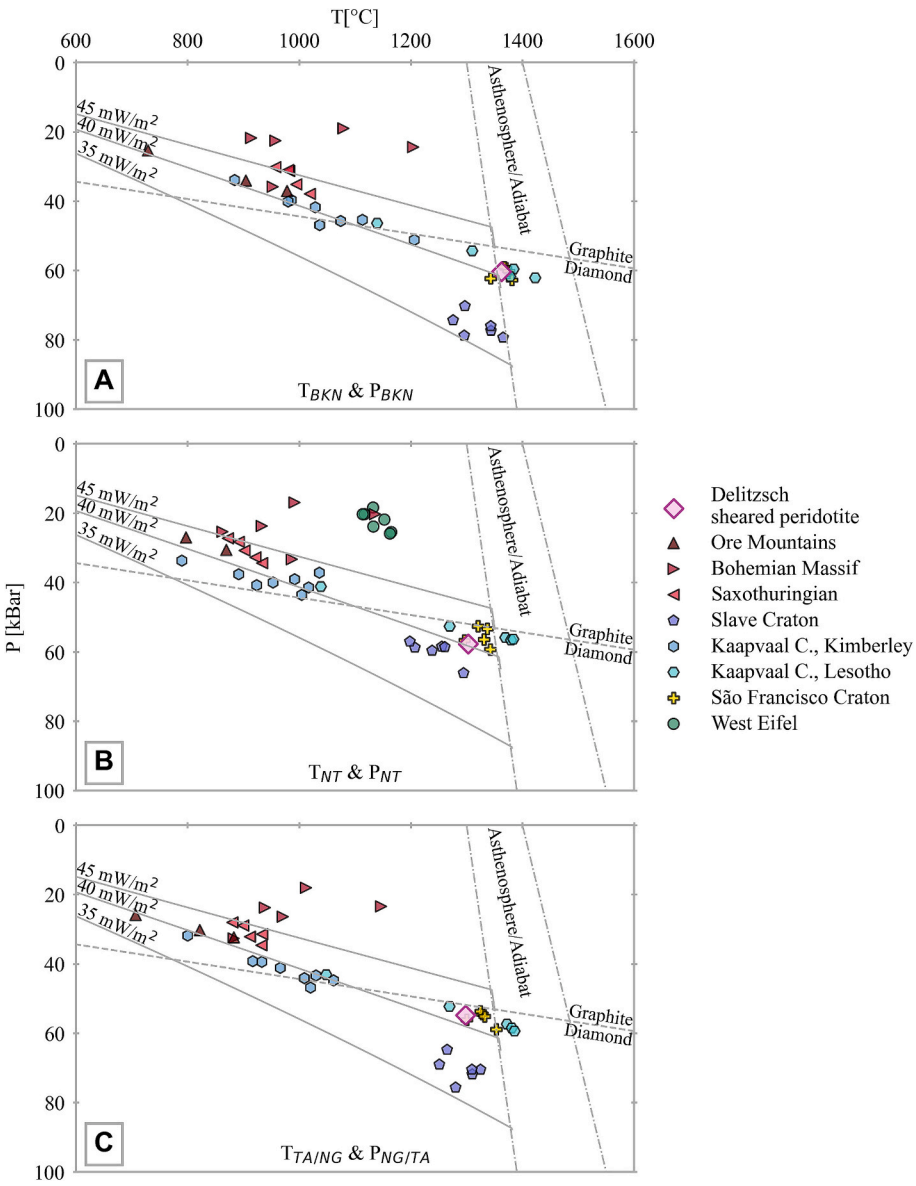

Fig. 14. Geothermometry and -barometry data for the Delitzsch sheared garnet peridotite calculated with different iteratively solved thermo- barometer combinations plotted alongside literature data (Braga et al., 2024; Heckel et al., 2023, 2022; Mather, 2012; Medaris et al., 2015, 2005; Schmädicke and Evans, 1997; Witt-Eickschen and Kramm, 1998). A: T_{BKN} & P_{BKN}: two-pyroxene thermometer T_{BKN} and garnet-orthopyroxene barometer P_{BKN}. B: T_{NT} & P_{NT}: Cr-in-clinopyroxene thermometer T_{NT} and enstatite-in-clinopyroxene barometer P_{NT}. C: $T_{TA/NG}$ & $P_{NG/TA}$: two-pyroxene thermometer T_{TA} and garnet-orthopyroxene barometer P_{NG}.

rather than the convection of the asthenosphere (Heckel et al., 2023). For our sample, it can be envisaged that deformation was due to interaction with the proto-UML melt at depth. It should be noted that, even in the case of linked ascent, metasomatism, and deformation, the xenolith would still originate from the LAB, given the high formation pressures and temperatures involved.

High-temperature metasomatism is indicated by the re-enrichment of trace elements, particularly MREE, Ti, and Cr (see chapter 4.3). Trace element concentrations in various mineral phases are influenced not only by temperature and pressure conditions but also by the geochemical properties and partitioning behavior of the elements (e.g., Henderson, 1984; Righter et al., 2014). Generally, immobile high field strength elements (HFSE), such as Nb, Ta, Zr and Hf, prefer to stay in the liquid phase, resulting in negative anomalies in the trace element plot (e.g., Fig. 12), shown in chapter 4.3. The HFSE and Ti abundances display a strong positive anomaly, which is likely linked to interaction with a high-temperature metasomatic agent, such as a CO_2-rich melt. In such a melt, the Ti solubility would be increased and lead to enrichment of the metasomatic agent (Heckel et al., 2023; Tappe et al., 2017) which would then further percolate and enrich the surrounding mantle rock (i.e., the Delitzsch sheared garnet lherzolite). Further evidence for high-temperature melt metasomatism is provided by the "normal" trace element patterns observed in garnet (Stachel et al., 2004).

During deformation, olivine recrystallized, preserving some of the directional strain in its texture. The mosaic texture is characterized by irregular grain boundaries, with only a few forming the preferred 120° triple junctions (Heckel et al., 2023). Fast recrystallization is further evidenced by the small grain size and the chaotic appearance of kink bands. Kink bands appear during the crystallization process at mantle depths (Green and Radcliffe, 1972) and suggest insufficient time for stress reduction.

A disequilibrium of 3.5 kbar (Table 5), equivalent to approximately 11 km, is observed between ortho- and clinopyroxene when using clinopyroxene rim values instead of core values. This disequilibrium is absent when comparing clinopyroxene cores to orthopyroxene, arguing for incipient re-equilibration at different conditions.

Table 6
Estimated modal composition based on pixel data and specific gravity of olivine (ol), clinopyroxene (cpx), orthopyroxene (opx), and garnet (grt).

Sample		**opx**	**cpx**	**ol**	**grt**	**Sum**
Section_1	amount [pixel]	5789	4741	20,184	4668	35,382
	amount [%]	16	13	57	13	100
Section_2	amount [pixel]	4365	5175	18,775	1905	30,220
	amount [%]	14	17	62	6	100
Sample_average	amount [%]	15	15	60	10	100
Sample		**opx**	**cpx**	**ol**	**grt**	**Sum**
Section_1	amount [pixel]	5789	4741	20,184	4668	35,382
	amount [%]	16	13	57	13	100
Section_2	amount [pixel]	4365	5175	18,775	1905	30,220
	amount [%]	14	17	62	6	100
Sample_average	amount [%]	15	15	60	10	100
Correction for specific gravites		**opx**	**cpx**	**ol**	**gt**	**Sum**
calculated specific gravities		3.23	2.90	3.34	3.74	
contributing mass per unit		0.50	0.44	1.99	0.36	3.30
modal composition [%]		15	13	60	11	100

Table 7
Calculated bulk composition (after McDonough and Rudnick (1998)).

Oxides	Primitive	Off-craton	On-craton	Dunite	This Study
[wt%]	Mantle	Lherzolite	Harzburgite	(89-774)	TR_bulk
SiO_2	45.00	44.16	43.80	41.30	44.62
TiO_2	0.20	0.09	0.08	0.00	0.20
Al_2O_3	4.45	2.25	0.56	0.10	2.85
Cr_2O_3	0.38	0.39	0.38	0.28	0.30
FeO	8.05	8.14	7.71	6.26	8.62
MnO	0.14	0.14	0.12	0.08	0.13
MgO	37.80	41.05	46.30	51.88	39.63
NiO	0.25	0.27	0.35	0.36	0.26
CaO	3.55	2.27	0.75	0.16	2.87
Na_2O	0.36	0.21	0.07	0.03	0.26
K_2O	0.03	0.02	0.03	0.02	0.01
Mg#	89.3	90.0	91.4	93.7	89.1

We interpret the 61.1 kbar (calculated with the clinopyroxene core values) to be the equilibrium lithostatic pressure, which is also supported by the textural and compositional equilibrium observed among the mineral phases. However, we cannot completely rule out the potential effect of additional pressure (e.g., by hydraulic forces) caused by melt interaction. The rapid ascent of the UML magma likely induced decompression melting in clinopyroxene, which is evidenced by the occurrence of spongy rims (Carpenter et al., 2002; Pan et al., 2018). Likewise, the kelyphite rims around garnet are probably the result of interaction with a melt during decompression (e.g., Canil and Fedortchouk, 1999; Spetsius and Taylor, 2002). Kelyphite rims around garnet likely formed during the ascent of the host UML magma. The transformation of garnet and olivine into amphibole and other mineral phases would have occurred at lower pressures. A possible interpretation of kelyphites is the (partial) retrograde metamorphism from high-pressure garnet peridotites to low-pressure spinel peridotites (Godard and Martin, 2000).

Veins likely formed in a later phase, representing remnants of alteration caused by fault systems disrupting the xenolith, as observed in carbonatitic rocks of the DCC (Loidolt et al., 2022).

5.4. Petrogenetic model

Literature about other sheared peridotites mainly focus on Archean thick lithosphere (Davis et al., 2003; Poujol et al., 2003). In this context, the formation and evolution of thick lithosphere is usually attributed to extensive melt depletion and lateral accretion, followed by refertilization by melts/fluids from below (e.g., Pearson et al., 2021).

In Germany, the current lithosphere structure around the Delitzsch area is well studied, with the Mohorovičić discontinuity (MOHO) being presently documented at depths between 35 and 40 km (Artemieva and Meissner, 2012; Kind et al., 2017) and the LAB presently at 120-140 km (Jones et al., 2010; Praus et al., 1990). While these depths accurately reflect the current lithosphere in Eastern Germany, they do not represent the past conditions during the formation of the DCC approximately 72–83 Ma (Möckel, 2023). While a present-day thinned Saxothuringian lithosphere was confirmed using S-receiver function analysis (Heuer et al., 2007), it remains ambiguous whether this thinning is related to tectonic activity during the Alpine Orogeny or if an earlier delamination is the more likely cause (Schulmann, 2002).

Assuming that the sheared garnet lherzolite reflects a sample of the past LAB at a depth of approximately 190 km, a difference in LAB depth of 50–70 km between the Cretaceous and present day can be calculated. While uplift and subsequent erosion have certainly influenced lithospheric thickness, those processes alone cannot account for the change in thickness. Erosion rates in the still rising Alps, averaging 0.6 mm/a (43.2 km in 72 Ma) (Champagnac et al., 2009), would not only be insufficient to explain the deficit but also unrealistic to be extrapolated over such a long period of time. For comparison, long-term erosion rates in the Argentine Precordillera average less than 0.1 mm/a (< 7.2 km in 72 Ma) (Val et al., 2016). Therefore, a different explanation must be found.

Similar thinning and lithospheric destruction to the Delitzsch subcontinental lithospheric mantle (SCLM) have been reported from the margins of the São Francisco Craton, Brazil (Braga et al., 2024), where a combination of tectonic activity, intruding melt, and interaction with the asthenosphere are believed to have driven the destabilization of the formerly thick lithospheric mantle. Given the similarities in setting and compositional data (see chapter 4), it is possible that similar processes affected the mantle below the Delitzsch region. Another well-documented example of SCLM destruction is the North China Craton, where subduction of the Pacific Plate is believed to have been the primary driver destabilizing the eastern portion of the cratonic root. This subduction event altered mantle flow dynamics, ultimately leading to the destabilization and thinning of the SCLM (Zhu et al., 2011). Lithospheric extension, interpreted as a response to these dynamic changes, has also been observed in the North China Craton (Liu et al., 2018). Notably, the lithospheric thickness beneath the eastern North China Craton must have decreased rapidly from ~200 km to ~35 km within approximately 10 million years (Chen et al., 2023). This dramatic thinning has been attributed to a combination of convective erosion, asthenospheric upwelling (Liu et al., 2018), and possibly catastrophic delamination (Chen et al., 2023).

Thus, multiple scenarios regarding the origin of the DCC sheared garnet lherzolite sample can be discussed. One scenario suggests an asthenospheric upwelling, proposing that, instead of sampling the LAB, the sample originates from the asthenosphere. Reactivation of old fault systems during the Alpine Orogeny led to upwelling, which caused the formation of the DCC (Krüger et al., 2013). An asthenospheric source for the sheared garnet lherzolite xenolith would explain its genetic similarity to both PRIMA and off-craton lherzolitic compositions (Table 7). Our olivine value of Mg# 89.4 closely matches the PRIMA Mg# of 89.3, either suggesting an origin from convecting primitive mantle or extensive refertilization of lithospheric material. In the case of refertilization, the following scenario would apply:

Given the absence of thick lithosphere in the region today, a model suggesting the former presence of thickened SCLM beneath the late Proterozoic to early Phanerozoic crust (Jones et al., 2010) is proposed here (Fig. 15). There is evidence for an increased crustal thickness (i.e., up to 70 km) in the area (i.e., Variscan hinterland) during the Paleozoic (Hillenbrand and Williams, 2022). Further support for a formerly thick lithosphere, originally produced during the Variscan orogeny, comes from a present-day seismic anomaly detected around N 51°-52° and E 12°, which potentially represents part of the delaminating lithosphere

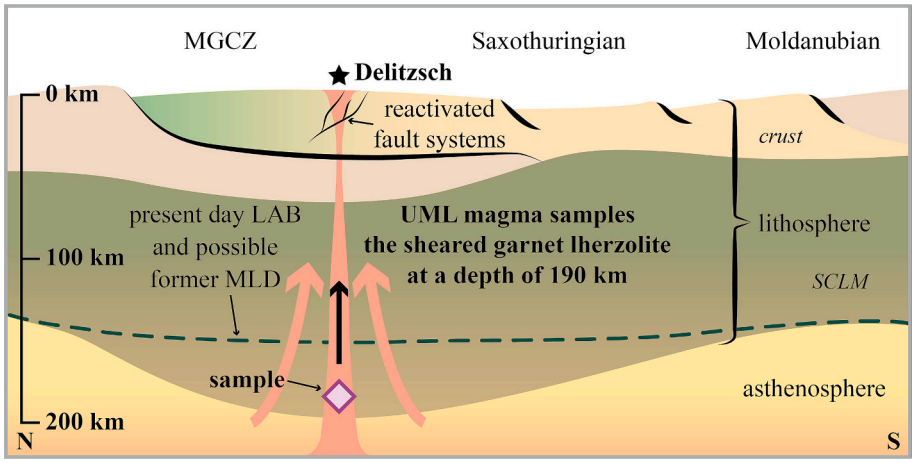

Fig. 15. Schematic cartoon showcasing the thick lithosphere model below Delitzsch during the late Cretaceous: The sheared garnet lherzolite is sampled during active destruction of the subcontinental lithospheric mantle (SCLM), whereas significant thinning of the lithosphere only occurred after this process took place. Delamination of the lower lithosphere may have occurred along a mid-lithospheric discontinuity (MLD). The star marks the location of the Delitzsch Carbonatite Complex (DCC), while the purple diamond represents the original location of the studied xenolith prior to its sampling by the host ultramafic lamprophyre (UML), of alnöite composition. The initial tectonic scenario reflects the post-Variscan orogeny state in central Europe (after 300 Ma). The abbreviation MGCZ used in the figure refers to the Mid-German Crystalline Zone and LAB to the lithosphere-asthenosphere boundary. (For interpretation of the references to colour in this figure legend, the reader is referred to the web version of this article.)

(Kind et al., 2017). In this model, the change in lithospheric thickness is explained by a combination of melt-induced metasomatism and thermal erosion (Braga et al., 2024), and subsequent delamination (O'Reilly and Griffin, 2010). In this scenario, the xenolith represents a sample from the LAB (i.e., a fragment of refertilized lower SCLM), and was entrained during the destabilization and destruction of the lower lithosphere.

One way of lithosphere destruction by delamination could be due to pargasite channels within the mantle lithosphere. These are horizontally aligned channels of amphibole that are hypothesized to be responsible for mid-lithospheric discontinuities, and as such could provide a plane of delamination for the lower lithospheric keel (Kovács et al., 2021; Sudholz et al., 2024). In summary, the destruction of formerly thick lithosphere below Delitzsch, left over after the Variscan orogeny, was likely promoted by a switch to extensional tectonics during the Alpine orogeny. It should be noted that carbonatite-UML-complexes are typically associated with continental extension (Tappe et al., 2006).

6. Conclusions

The sheared garnet peridotite xenolith from the Delitzsch Carbonatite Complex is the first mantle-derived garnet-peridotite recovered in Germany and exhibits a mosaic porphyroclastic texture with pyroxene and garnet porphyroclasts embedded in a matrix of olivine neoblasts. The evaluation of the measured data confirms high-temperature (1330 °C) and high-pressure (61.1 kbar) mineral-melt interactions. A fertile mantle source is indicated with (re-)enrichment of key trace elements such as Ti and Cr in the sheared peridotite. The presence of small fluidal-mosaic olivine neoblasts, kelyphite rims around garnet, and minor zoning as well as spongy rims around clinopyroxene suggest rapid ascent accompanied by interaction with a CO_2-rich melt, a process also observed in kimberlites within cratons. Barometric analysis indicates that the formation occurred at a depth of 190 km well below the current lithosphere-asthenosphere boundary. With a bulk Mg# of 89.1 and overall chemical composition closely resembling primitive or lherzolitic compositions, an origin from the asthenosphere cannot entirely be ruled out. In this scenario, a possible exhumation mechanism could involve asthenospheric upwelling, driven by extensional tectonics during the Alpine orogeny. Another possibility, preferred here, is the presence of a formerly thick lithosphere left over after the Variscan orogeny, with the xenolith being sampled during destruction of the lower lithosphere. Melt-induced destabilization and a combination of uplift and significant erosion of the upper crust could explain the difference in lithospheric thickness between the time of emplacement (late Cretaceous) and present day. This model carries profound implications for understanding the regional mantle processes and tectonic history, e.g. that thickened lithosphere existed at least until the late Cretaceous. Further studies on the area around the DCC, particularly focused on sheared garnet peridotite samples and isotopic studies, could help to provide more definitive answers.

Supplementary data to this article can be found online at https://doi.org/10.1016/j.lithos.2025.108156.

Declaration of competing interest

The authors declare that they have no known competing financial interests or personal relationships that could have appeared to influence the work reported in this paper.

Acknowledgements

Kathrin Jung is thanked for preparing the thick sections at the University of Cologne. Prof. Thomas Stachel at the University of Alberta, Canada is thanked for discussion of the PTEXL results. Nadia Malaspina is thanked for efficient editorial handling. Istvan Kovács and Igor Ashchepkov are thanked for their detailed and helpful comments.

References

Ackerman, L., Mahlen, N., JelInek, E., Medaris, G., Ulrych, J., Strnad, L., MihaljeviC, M., 2007. Geochemistry and Evolution of Subcontinental Lithospheric Mantle in Central Europe: evidence from Peridotite Xenoliths of the Kozakov Volcano, Czech Republic. J. Petrol. 48, 2235–2260. https://doi.org/10.1093/petrology/egm058.

Artemieva, I.M., Meissner, R., 2012. Crustal thickness controlled by plate tectonics: a review of crust–mantle interaction processes illustrated by European examples. Tectonophysics 530–531, 18–49. https://doi.org/10.1016/j.tecto.2011.12.037.

Ashchepkov, I.V., André, L., Downes, H., Belyatsky, B.A., 2011. Pyroxenites and megacrysts from Vitim picrite-basalts (Russia): Polybaric fractionation of rising melts in the mantle? J. Asian Earth Sci. 42, 14–37. https://doi.org/10.1016/j.jseaes.2011.03.004.

Boyd, F.R., Nixon, P.H., 1975. Origins of the ultramafic nodules from some kimberlites of northern Lesotho and the Monastery Mine, South Africa. Phys. Chem. Earth 9, 431–454. https://doi.org/10.1016/0079-1946(75)90032-4.

Boyd, F.R., Nixon, P.H., 1978. Ultramafic nodules from the Kimberley pipes, South Africa. Geochim. Cosmochim. Acta 42, 1367–1382. https://doi.org/10.1016/0016-7037(78)90042-X.

Braga, L.G., Jalowitzki, T., Gervasoni, F., Rodrigues, R.F., Mazzucchelli, M., Giovanardi, T., Costa, M.M.D., Santos, R.V., Rocha, M.P., Fuck, R.A., Lorenzoni, G. R., Bertotto, G.W., 2024. Destruction of the Lithosphere beneath the SW margin of the São Francisco Craton Evidenced by Refertilized and Deformed Mantle Xenoliths. J. Petrol. 65. https://doi.org/10.1093/petrology/egae087.

Brey, G.P., Köhler, T., 1990. Geothermobarometry in Four-phase Lherzolites II. New Thermobarometers, and Practical Assessment of existing Thermobarometers. J. Petrol. 31, 1353–1378. https://doi.org/10.1093/petrology/31.6.1353.

Bussweiler, Y., Brey, G.P., Pearson, D.G., Stachel, T., Stern, R.A., Hardman, M.F., Kjarsgaard, B.A., Jackson, S.E., 2017. The aluminum-in-olivine thermometer for mantle peridotites — Experimental versus empirical calibration and potential applications. Lithos 272–273, 301–314. https://doi.org/10.1016/j.lithos.2016.12.015.

Bussweiler, Y., Giuliani, A., Greig, A., Kjarsgaard, B.A., Petts, D., Jackson, S.E., Barrett, N., Luo, Y., Pearson, D.G., 2019. Trace element analysis of high-Mg olivine by LA-ICP-MS – Characterization of natural olivine standards for matrix-matched calibration and application to mantle peridotites. Chem. Geol. 524, 136–157. https://doi.org/10.1016/j.chemgeo.2019.06.019.

Canil, D., Fedortchouk, Y., 1999. Garnet dissolution and the emplacement of kimberlites. Earth Planet. Sci. Lett. 167, 227–237. https://doi.org/10.1016/S0012-821X(99)00019-9.

Cao, L.-T., Zheng, J.-P., Dai, H.-K., Xiong, Q., Lin, A.-B., Pan, S.-K., 2023. Fertile mantle domains with different metasomatic features beneath the eastern North China Craton: Transformation from variably auto-metasomatized asthenospheric upwelling. Lithos 454–455, 107259. https://doi.org/10.1016/j.lithos.2023.107259.

Carpenter, R.L., Edgar, A.D., Thibault, Y., 2002. Origin of spongy textures in clinopyroxene and spinel from mantle xenoliths, Hessian Depression, Germany. Mineral. Petrol. 74, 149–162. https://doi.org/10.1007/s007100200002.

Champagnac, J.-D., Schlunegger, F., Norton, K., von Blanckenburg, F., Abbühl, L.M., Schwab, M., 2009. Erosion-driven uplift of the modern Central Alps. Tectonophysics 474, 236–249. https://doi.org/10.1016/j.tecto.2009.02.024.

Chen, H., Tang, M., Song, S., 2023. Catastrophic craton destruction via wholesale lithosphere delamination. Geology 51, 460–464. https://doi.org/10.1130/G50803.1.

Clarke, D.B., Pe, G.G., Mackay, R.M., Gill, K.R., O'Hara, M.J., Gard, J.A., 1977. A new potassium-iron-nickel sulphide from a nodule in kimberlite. Earth Planet. Sci. Lett. 35, 421–428. https://doi.org/10.1016/0012-821X(77)90075-9.

Davis, W.J., Jones, A.G., Bleeker, W., Grütter, H., 2003. Lithosphere development in the Slave craton: a linked crustal and mantle perspective. Lithos 71, 575–589. https://doi.org/10.1016/S0024-4937(03)00131-2.

De Hoog, J.C.M., Gall, L., Cornell, D.H., 2010. Trace-element geochemistry of mantle olivine and application to mantle petrogenesis and geothermobarometry. Chem. Geol. 270, 196–215. https://doi.org/10.1016/j.chemgeo.2009.11.017.

Franke, W., 2000. The mid-European segment of the Variscides: tectonostratigraphic units, terrane boundaries and plate tectonic evolution. Geol. Soc. Lond. Spec. Publ. 179, 35–61. https://doi.org/10.1144/GSL.SP.2000.179.01.05.

Franke, W., 2006. The Variscan orogen in Central Europe: construction and collapse. Geol. Soc. Lond. Mem. 32, 333–343. https://doi.org/10.1144/GSL.MEM.2006.032.01.20.

Godard, G., Martin, S., 2000. Petrogenesis of kelyphites in garnet peridotites: a case study from the Ulten zone, Italian Alps. J. Geodyn. 30, 117–145. https://doi.org/10.1016/S0264-3707(99)00030-7.

Green, H.W., Radcliffe, S.V., 1972. Dislocation mechanisms in olivine and flow in the upper mantle. Earth Planet. Sci. Lett. 15, 239–247. https://doi.org/10.1016/0012-821X(72)90169-0.

Grütter, H.S., Gurney, J.J., Menzies, A.H., Winter, F., 2004. An updated classification scheme for mantle-derived garnet, for use by diamond explorers. Lithos 77, 841–857. https://doi.org/10.1016/j.lithos.2004.04.012.

Harte, B., 1977. Rock Nomenclature with Particular Relation to Deformation and Recrystallisation Textures in Olivine-Bearing Xenoliths. J. Geol. 85, 279–288. https://doi.org/10.1086/628299.

Hasterok, D., Chapman, D.S., 2011. Heat production and geotherms for the continental lithosphere. Earth Planet. Sci. Lett. 307, 59–70. https://doi.org/10.1016/j.epsl.2011.04.034.

Heckel, C., Woodland, A.B., Linckens, J., Gibson, S.A., Seitz, H.-M., 2022. Sheared Peridotites from Kimberley (Kaapvaal Craton, RSA): Record of Multiple Metasomatic events Accompanied with Deformation. J. Petrol. 63. https://doi.org/10.1093/petrology/egac096.

Heckel, C., Woodland, A.B., Linckens, J., Gibson, S.A., Seitz, H.M., 2023. Sheared Peridotites from Northern Lesotho: Metasomatism-Induced Deformation and Craton Destabilization. J. Petrol. 64. https://doi.org/10.1093/petrology/egad076.

Henderson, P., 1984. General Geochemical Properties and Abundances of the Rare Earth Elements. In: Developments in Geochemistry. Elsevier, pp. 1–32. https://doi.org/10.1016/B978-0-444-42148-7.50006-X.

Heuer, B., Kämpf, H., Kind, R., Geissler, W.H., 2007. Seismic evidence for whole lithosphere separation between Saxothuringian and Moldanubian tectonic units in Central Europe. Geophys. Res. Lett. 34. https://doi.org/10.1029/2006GL029188.

Hillenbrand, I.W., Williams, M.L., 2022. Geochemical evidence for Diachronous Uplift and Synchronous Collapse of the High Elevation Variscan Hinterland. Geophys. Res. Lett. 49. https://doi.org/10.1029/2022GL100435.

Hu, Z., Liu, Y., Gao, S., Xiao, S., Zhao, L., Günther, D., Li, M., Zhang, W., Zong, K., 2012. A "wire" signal smoothing device for laser ablation inductively coupled plasma mass spectrometry analysis. Spectrochim Acta Part B At Spectrosc 78, 50–57. https://doi.org/10.1016/j.sab.2012.09.007.

Jochum, K.P., Stoll, B., Herwig, K., Willbold, M., Hofmann, A.W., Amini, M., Aarburg, S., Abouchami, W., Hellebrand, E., Mocek, B., Raczek, I., Stracke, A., Alard, O., Bouman, C., Becker, S., Dücking, M., Brätz, H., Klemd, R., de Bruin, D., Canil, D., Cornell, D., de Hoog, C., Dalpé, C., Danyushevsky, L., Eisenhauer, A., Gao, Y., Snow, J.E., Groschopf, N., Günther, D., Latkoczy, C., Guillong, M., Hauri, E.H., Höfer, H.E., Lahaye, Y., Horz, K., Jacob, D.E., Kasemann, S.A., Kent, A.J.R., Ludwig, T., Zack, T., Mason, P.R.D., Meixner, A., Rosner, M., Misawa, K., Nash, B.P., Pfänder, J., Premo, W.R., Sun, W.D., Tiepolo, M., Vannucci, R., Vennemann, T., Wayne, D., Woodhead, J.D., 2006. MPI-DING reference glasses for in situ microanalysis: New reference values for element concentrations and isotope ratios. Geochem. Geophys. Geosyst. 7. https://doi.org/10.1029/2005GC001060.

Johnson, G.R., Olhoeft, G.R., 1984. Density of Rocks and Minerals. In: Handbook of Physical Properties of Rocks. CRC Press, pp. 1–38.

Jones, A.G., Plomerova, J., Korja, T., Sodoudi, F., Spakman, W., 2010. Europe from the bottom up: a statistical examination of the central and northern European lithosphere–asthenosphere boundary from comparing seismological and electromagnetic observations. Lithos 120, 14–29. https://doi.org/10.1016/j.lithos.2010.07.013.

Kargin, A.V., Sazonova, L.V., Nosova, A.A., Pervov, V.A., Minevrina, E.V., Khvostikov, V. A., Burmii, Z.P., 2017. Sheared peridotite xenolith from the V. Grib kimberlite pipe, Arkhangelsk Diamond Province, Russia: Texture, composition, and origin. Geosci. Front. 8, 653–669. https://doi.org/10.1016/j.gsf.2016.03.001.

Kargin, A., Bussweiler, Y., Nosova, A., Sazonova, L., Berndt, J., Klemme, S., 2021. Titanium-rich metasomatism in the lithospheric mantle beneath the Arkhangelsk Diamond Province, Russia: insights from ilmenite-bearing xenoliths and HP–HT reaction experiments. Contrib. Mineral. Petrol. 176, 101. https://doi.org/10.1007/s00410-021-01863-9.

Kind, R., Handy, M.R., Yuan, X., Meier, T., Kämpf, H., Soomro, R., 2017. Detection of a new sub-lithospheric discontinuity in Central Europe with S-receiver functions. Tectonophysics 700–701, 19–31. https://doi.org/10.1016/j.tecto.2017.02.002.

Konopásek, J., Schulmann, K., 2005. Contrasting early Carboniferous field geotherms: evidence for accretion of a thickened orogenic root and subducted Saxothuringian crust (central European Variscides). J. Geol. Soc. Lond. 162, 463–470. https://doi.org/10.1144/0016-764904-004.

Kovács, I.J., Liptai, N., Koptev, A., Cloetingh, S.A.P.L., Lange, T.P., Mațenco, L., Szakács, A., Radulian, M., Berkesi, M., Patkó, L., Molnár, G., Novák, A., Wesztergom, V., Szabó, C., Fancsik, T., 2021. The 'pargasosphere' hypothesis: looking at global plate tectonics from a new perspective. Glob. Planet. Chang. 204, 103547. https://doi.org/10.1016/j.gloplacha.2021.103547.

Krogh, E.J., 1988. The garnet-clinopyroxene Fe-Mg geothermometer - a reinterpretation of existing experimental data. Contrib. Mineral. Petrol. 99, 44–48. https://doi.org/10.1007/BF00399364.

Kroner, U., Romer, R.L., 2013. Two plates — many subduction zones: the Variscan orogeny reconsidered. Gondwana Res. 24, 298–329. https://doi.org/10.1016/j.gr.2013.03.001.

Krüger, J.C., Romer, R.L., Kämpf, H., 2013. Late Cretaceous ultramafic lamprophyres and carbonatites from the Delitzsch Complex, Germany. Chem. Geol. 353, 140–150. https://doi.org/10.1016/j.chemgeo.2012.09.026.

Liu, L., Morgan, J.P., Xu, Y., Menzies, M., 2018. Craton Destruction 2: Evolution of Cratonic Lithosphere after a Rapid Keel Delamination Event. J. Geophys. Res. Solid Earth 123. https://doi.org/10.1029/2017JB015374.

Loidolt, C., Zimmermann, R., Tusa, L., Lorenz, S., Ebert, D., Gloaguen, R., Broom-Fendley, S., 2022. New Insights into the rare Earth Element Mineralization of the Storkwitz Carbonatite, Germany. Can. Mineral. 60, 913–932. https://doi.org/10.3749/canmin.2100061.

Massonne, H.-J., 1998. A new occurrence of microdiamonds in quartzofeldspathic rocks of the Saxonian Erzgebirge, Germany, and their metamorphic evolution. In: International Kimberlite Conference Extended Abstracts. University of Alberta, pp. 552–554. https://doi.org/10.29173/ikc2801.

Mather, K.A., 2012. A Xenolith-Based Lithospheric Transect of the Slave Craton. Durham University, N.W.T., Canada (Doctoral dissertation).

McDonough, W.F., Rudnick, R.L., 1998. Chapter 4. Mineralogy and composition of the upper mantle. In: Ultrahigh Pressure Mineralogy. De Gruyter, pp. 139–164. https://doi.org/10.1515/9781501509179-006.

Medaris, G., Wang, H., Jelínek, E., Mihaljevič, M., Jakeš, P., 2005. Characteristics and origins of diverse Variscan peridotites in the Gföhl Nappe, Bohemian Massif, Czech Republic. Lithos 82, 1–23. https://doi.org/10.1016/j.lithos.2004.12.004.

Medaris, G., Ackerman, L., Jelínek, E., Toy, V., Siebel, W., Tikoff, B., 2012. The Sklené garnet peridotite: petrology, geochemistry, and structure of a mantle-derived boudin in Moldanubian granulite. J. Geosci. 301–323. https://doi.org/10.3190/jgeosci.052.

Medaris, G., Ackerman, L., Jelínek, E., Michels, Z.D., Erban, V., Kotková, J., 2015. Depletion, cryptic metasomatism, and modal metasomatism (refertilization) of Variscan lithospheric mantle: evidence from major elements, trace elements, and Sr-Nd-Os isotopes in a Saxothuringian garnet peridotite. Lithos 226, 81–97. https://doi.org/10.1016/j.lithos.2014.10.007.

Mercier, J.-C.C., 1979. Peridotite xenoliths and the dynamics of kimberlite intrusion. In: The Mantle Sample: Inclusion in Kimberlites and Other Volcanics. American Geophysical Union, Washington, D. C, pp. 197–212. https://doi.org/10.1029/SP016p0197.

Möckel, F., 2023. Der Delitzsch Karbonatit-Komplex. Geoprofil des LfULG Heft 17, 80–136.

Morimoto, N., 1988. Nomenclature of Pyroxenes. Mineral. Petrol. 39, 55–76. https://doi.org/10.1007/BF01226262.

Muriuki, J., Nakamura, D., Hirajima, T., Svojtka, M., 2020. Mineralogical heterogeneity of UHP garnet peridotite in the Moldanubian Zone of the Bohemian Massif (Nové Dvory, Czech Republic). J. Mineral. Petrol. Sci. 115, 1–20. https://doi.org/10.2465/jmps.190126.

Nickel, K.G., Green, D.H., 1985. Empirical geothermobarometry for garnet peridotites and implications for the nature of the lithosphere, kimberlites and diamonds. Earth Planet. Sci. Lett. 73, 158–170. https://doi.org/10.1016/0012-821X(85)90043-3.
Nimis, P., Taylor, W.R., 2000. Single clinopyroxene thermobarometry for garnet peridotites. Part I. Calibration and testing of a Cr-in-Cpx barometer and an enstatite-in-Cpx thermometer. Contrib. Mineral. Petrol. 139, 541–554. https://doi.org/10.1007/s004100000156.
Nimis, P., Preston, R., Perritt, S.H., Chinn, I.L., 2020. Diamond's depth distribution systematics. Lithos 376–377, 105729. https://doi.org/10.1016/j.lithos.2020.105729.
Nimis, P., Zanetti, A., Franz, L., 2024. A revision of the Ni-in-garnet geothermometer with special regard to its pressure dependence. Lithos 468–469, 107513. https://doi.org/10.1016/j.lithos.2024.107513.
O'Reilly, S.Y., Griffin, W.L., 2010. The continental lithosphere–asthenosphere boundary: can we sample it? Lithos 120, 1–13. https://doi.org/10.1016/j.lithos.2010.03.016.
Palme, H., O'Neill, H.St.C., 2014. Cosmochemical Estimates of Mantle Composition. In: Treatise on Geochemistry. Elsevier, pp. 1–39. https://doi.org/10.1016/B978-0-08-095975-7.00201-1.
Pan, S., Zheng, J., Yin, Z., Griffin, W.L., Xia, M., Lin, A., Zhang, H., 2018. Spongy texture in mantle clinopyroxene recordsdecompression-induced melting. Lithos 320–321, 144–154. https://doi.org/10.1016/j.lithos.2018.08.035.
Pearson, D.G., Scott, J.M., Liu, J., Schaeffer, A., Wang, L.H., van Hunen, J., Szilas, K., Chacko, T., Kelemen, P.B., 2021. Deep continental roots and cratons. Nature 596, 199–210. https://doi.org/10.1038/s41586-021-03600-5.
Poujol, M., Robb, L.J., Anhaeusser, C.R., Gericke, B., 2003. A review of the geochronological constraints on the evolution of the Kaapvaal Craton, South Africa. Precambrian Res. 127, 181–213. https://doi.org/10.1016/S0301-9268(03)00187-6.
Praus, O., Pěčová, J., Petr, V., Babuška, V., Plomerová, J., 1990. Magnetotelluric and seismological determination of the lithosphere-asthenosphere transition in Central Europe. Phys. Earth Planet. Inter. 60, 212–228. https://doi.org/10.1016/0031-9201(90)90262-V.
Ramsay, R.R., 1992. Geochemistry of Diamond indicator Minerals (Doctoral dissertation).. University of Western Australia.
Righter, K., Danielson, L., Drake, M.J., Domanik, K., 2014. Partition Coefficients at High Pressure and Temperature. In: Treatise on Geochemistry. Elsevier, pp. 449–477. https://doi.org/10.1016/B978-0-08-095975-7.00210-2.
Schmädicke, E., Evans, B.W., 1997. Garnet-bearing ultramafic rocks from the Erzgebirge, and their relation to other settings in the Bohemian Massif. Contrib. Mineral. Petrol. 127, 57–74. https://doi.org/10.1007/s004100050265.
Schulmann, K., 2002. Rapid burial and exhumation during orogeny: Thickening and synconvergent exhumation of thermally weakened and thinned crust (Variscan orogen in Western Europe). Am. J. Sci. 302, 856–879. https://doi.org/10.2475/ajs.302.10.856.
Seifert, W., 2000. Compositional variation in apatite, phlogopite and other accessory minerals of the ultramafic Delitzsch complex, Germany: implication for cooling history of carbonatites. Lithos 53, 81–100. https://doi.org/10.1016/S0024-4937(00)00010-4.
Spetsius, Z.V., Taylor, L.A., 2002. Partial Melting in Mantle Eclogite Xenoliths: Connections with Diamond Paragenesis. Int. Geol. Rev. 44, 973–987. https://doi.org/10.2747/0020-6814.44.11.973.
Stachel, T., 2022. PTEXL - Geothermobarometry of Mantle Rocks doi/10.5683/SP3/IMYNCL.
Stachel, T., Viljoen, K.S., Brey, G., Harris, J.W., 1998. Metasomatic processes in lherzolitic and harzburgitic domains of diamondiferous lithospheric mantle: REE in garnets from xenoliths and inclusions in diamonds. Earth Planet. Sci. Lett. 159, 1–12. https://doi.org/10.1016/S0012-821X(98)00064-8.
Stachel, T., Aulbach, S., Brey, G.P., Harris, J.W., Leost, I., Tappert, R., Viljoen, K.S., Fanus, 2004. The trace element composition of silicate inclusions in diamonds: a review. Lithos 77, 1–19. https://doi.org/10.1016/j.lithos.2004.03.027.
Sudholz, Z.J., Green, D.H., Yaxley, G.M., Jaques, A.L., 2022. Mantle geothermometry: experimental evaluation and recalibration of Fe–Mg geothermometers for garnet-clinopyroxene and garnet-orthopyroxene in peridotite, pyroxenite and eclogite systems. Contrib. Mineral. Petrol. 177, 77. https://doi.org/10.1007/s00410-022-01944-3.
Sudholz, Z.J., Zhang, P., Eakin, C.M., Yaxley, G.M., Jaques, A.L., Frigo, C., Czarnota, K., 2024. Ancient Craton-Wide Mid-Lithosphere Discontinuity Controlled by Pargasite Channels. Geophys. Res. Lett. 51. https://doi.org/10.1029/2024GL108433.
Tappe, S., Foley, S.F., Jenner, G.A., Heaman, L.M., Kjarsgaard, B.A., Romer, R.L., Stracke, A., Joyce, N., Hoefs, J., 2006. Genesis of Ultramafic Lamprophyres and Carbonatites at Aillik Bay, Labrador: a consequence of Incipient Lithospheric Thinning beneath the North Atlantic Craton. J. Petrol. 47, 1261–1315. https://doi.org/10.1093/petrology/egl008.
Tappe, S., Romer, R.L., Stracke, A., Steenfelt, A., Smart, K.A., Muehlenbachs, K., Torsvik, T.H., 2017. Sources and mobility of carbonate melts beneath cratons, with implications for deep carbon cycling, metasomatism and rift initiation. Earth Planet. Sci. Lett. 466, 152–167. https://doi.org/10.1016/j.epsl.2017.03.011.
Taylor, W.R., Nimis, P., 1998. A single-pyroxene thermobarometer for Iherzolitic Cr-diopside and its application in diamond exploration, in: International Kimberlite Conference Extended Abstracts: 1998. University of Alberta. https://doi.org/10.29173/ikc2923.
Val, P., Hoke, G.D., Fosdick, J.C., Wittmann, H., 2016. Reconciling tectonic shortening, sedimentation and spatial patterns of erosion from 10Be paleo-erosion rates in the argentine Precordillera. Earth Planet. Sci. Lett. 450, 173–185. https://doi.org/10.1016/j.epsl.2016.06.015.
Witt-Eickschen, G., Kramm, U., 1998. Evidence for the multiple stage evolution of the subcontinental lithospheric mantle beneath the Eifel (Germany) from pyroxenite and composite pyroxenite/peridotite xenoliths. Contrib. Mineral. Petrol. 131, 258–272. https://doi.org/10.1007/s004100050392.
Zhu, R., Chen, L., Wu, F., Liu, J., 2011. Timing, scale and mechanism of the destruction of the North China Craton. Sci. China Earth Sci. 54, 789–797. https://doi.org/10.1007/s11430-011-4203-4.